RRS-042

Reusable Reentry Satellite (RRS) Summary Report

Configuration Trade Study

December 1990

Contract NAS9-18202
DRL 02

Prepared for:

National Aeronautics and Space Administration
Lyndon B. Johnson Space Center
Houston, Texas 77058

SAIC®
Science Applications International Corporation
An Employee Owned Company
21151 Western Avenue • Torrance, California 90501 • (213) 781-9022

FOREWORD

The Reusable Reentry Satellite (RRS) Configuration Trade Study described herein was performed during Part 1 of the RRS Phase B contract. This report is one of several that describes the results of various trade studies performed to arrive at a recommended design for the RRS satellite system.

The overall RRS Phase B Study objective is to design a relatively inexpensive satellite to access space for extended periods of time, with eventual recovery of experiments on Earth. The expected principal use for such a system is research on the effects of variable gravity (0-1.5 g) and radiation on small animals, plants, lower life forms, tissue samples, and materials processes. The RRS will be capable of: 1) being launched by a variety of expendable launch vehicles, 2) operating in low earth orbit as a free flying unmanned laboratory, and 3) executing an independent atmospheric reentry and soft landing. The RRS will be designed to be refurbished and reused up to three times a year for a period of 10 years.

The information provided in this report describes the process involved in the evolution of the RRS overall configuration. This process considered reentry aerodynamics, aerothermodynamics, internal equipment layout, and vehicle mass properties. This report delineates the baseline design decisions that were used to initiate the RRS design effort. As a result, there will be deviations between this report and the RRS Final Report. In those instances, the RRS Final Report shall be considered to be the definitive reference.

The study was performed under the contract technical direction of Mr. Robert Curtis, SAIC Program Manager. The Configuration Trade study was directed by Mr. Steve Apfel of SAIC, who was assisted by Mr Sid Weinberg and Mr. William Loomis, also of SAIC. Mr. Michael Richardson, JSC New Initiatives Office, provided the RRS objectives and policy guidance for the performance of these tasks under the NAS 9-18202 contract.

CONTENTS

Section			Page
List of Abbreviations and Acronyms			iv
1.0	INTRODUCTION		1
	1.1	Background	1
	1.2	NASA JSC Statement of Work Task Definition	1
	1.3	Scope	4
2.0	STUDY APPROACH		4
	2.1	Organization	4
	2.2	Document Format	4
3.0	PURPOSE		5
4.0	GROUNDRULES AND ASSUMPTIONS		5
5.0	DESIGN OPTIONS AND DATA		6
	5.1	Top-Level Shape Options	7
	5.2	Initial RRV Mass Properties	9
6.0	AERODYNAMIC ANALYSIS		9
	6.1	Aerodynamic Stability	10
	6.2	Aerothermodynamics	13
	6.3	Analysis Results	14
7.0	STRUCTURAL ANALYSIS		18
	7.1	Layout of Vehicle Subsystems	18
		7.1.1 Payload	19
		7.1.2 Propulsion	19
		7.1.3 Power	21
		7.1.4 Thermal	25
		7.1.5 Electronics	25
		7.1.6 Terminal Recovery System	25
	7.2	Main Structure	25
		7.2.1 Loads	26
		7.2.2 Design Criteria	26
		7.2.3 Configuration Structural Design	26
	7.3	Structural Design Analysis	29
	7.4	Equipment Supports	35
	7.5	Nose Cap	36
	7.6	Astromast Dynamics	38
8.0	CONCLUSIONS/RECOMMENDATIONS		44

List of Tables

Section		Page
4-1	Top Level RRS Requirements Affecting Shape Selection	6
7-1	Material Properties for 6061-T6 Aluminum	29

List of Figures

Section		Page
5-1	Top-Level RRS Shape Options	8
6-1	Center of Pressure vs. Cone Angle and Bluntness Ratio	11
6-2	Configuration Evolution Methodology	15
6-3	Configuration Evolution	16
6-4	Reentry Loads Versus De-orbit Maneuver	17
6-5	Results—Examples of Net Heating Rates Predicted by SLAPEM	18
7-1	Fuel Cell Design	22
7-2	Battery Design	23
7-3	Solar Power Design	24
7-4	RRS Top View	27
7-5	Arrangement of Primary and Secondary Thrust Beams	27
7-6	Forward Conical Shell Dimensions	30
7-7	Typical Intermediate Frame Cross-Section	30
7-8	Structural Mass	31
7-9	Radial Shear Web Geometry	32
7-10	Attachment of Radial Shear Web to Payload Canister and External Shell	33
7-11	Shear Web Cap/Truss System	34
7-12	Payload Support	36
7-13	Nose Cap Design	37
7-14	Crush Distance Versus Honeycomb Crushing Stress	39
7-15	Dynamic Loading Analysis Model	40
7-16	Structural Deformation Results	43
7-17	Structural Deformation Results - Detailed View	43
7-18	Comparison of Longeron Loads With Allowables	44

References **45**

List of Abbreviations and Acronyms

3DSAP	3-D Shock and Pressure
CFD	Computational Fluid Dynamics
DRM	Design Reference Mission
ECLSS	Environmental Control and Life Support System
GN&C	Guidance, Navigation and Control
HBI	Heat Balance Integral
L/D	Lift-Over Drag
MS	Margin of Safety
NASA	National Aeronautics and Space Administration
PM	Payload Module
RRS	Reusable Reentry Satellite
RRV	Reusable Reentry Vehicle
SAIC	Science Applications International Corporation
SRD	Systems Requirement Document
TT&C	Telemetry, Tracking and Command

1.0 INTRODUCTION

1.1 Background

As currently conceived, the Reusable Reentry Satellite (RRS) will be designed to provide investigators, in several biological disciplines, with a relatively inexpensive method to access space for up to 60 days with eventual recovery on Earth. The RRS will be designed to permit totally intact, relatively soft, recovery of the vehicle, system refurbishment, and reflight with new and varied payloads. The RRS system will be capable of three reflights per year over a 10-year program lifetime. The RRS vehicle will have a large and readily accessible volume near the vehicle center of gravity for the Payload Module (PM) containing the experiment hardware. The vehicle is configured to permit the experimenter late access to the PM prior to launch and rapid access following recovery.

The RRS will operate as a free-flying spacecraft in orbit and be allowed to drift in attitude to provide an acceleration environment of less than 10^{-5} g. The acceleration environment during orbital trim maneuvers will be less than 10^{-3} g. The RRS is also configured to spin at controlled rates to provide an artificial gravity of up to 1.5 Earth g. The RRS system will be designed to be rugged, easily maintained, and economically refurbishable for the next flight. Some systems may be designed to be replaced, rather than refurbished, if cost effective and capable of meeting the specified turnaround time. The minimum time between recovery and reflight will be approximately 60 days. The PMs will be designed to be relatively autonomous, with experiments that require few commands and limited telemetry. Mass storage, if needed, will be accommodated in the PM. The hardware development and implementation phase is expected to begin in 1991 with a first launch in 1993.

Numerous trade studies and RRS functional design descriptions are required to define a viable RRS concept that satisfies the requirements. The National Aeronautics and Space Administration (NASA) has contracted with Science Applications International Corporation (SAIC) to perform a Phase B study to provide the RRS concept definition. The RRS Configuration Trade Study described in this report is one of the supporting study analyses performed by the SAIC team.

1.2 NASA JSC Statement of Work Task Definition

The Configuration Trade Study was performed per direction of the RRS Statement of Work and the System Requirements Document (SRD) as given in the following paragraphs:

General:

SOW paragraph 3.1.2.1 RRS, RM and EBF Size and Configuration. Conduct the following tradeoff studies associated with selection of the optimum RRS size and configuration:

(a) Consider the size of the RRS from the minimum required to accommodate the RM or EBF to a maximum that can be accommodated by the prospective launch vehicles. All RRS designs shall be balanced with an adequate aerodynamic static margin and oblate and symmetric inertia characteristics about the vehicle longitudinal axis.

(b) Determine overall RRS mass, complexity, costs (development, first unit and refurbishment), and other pertinent parameters for the selected sizes and configurations.

(c) Determine the mission impacts/constraints and payload benefits associated with the various choices of sizes, configurations, and launch vehicles.

(d) Consider the effect of choice of launch vehicle on the tradeoffs, e.g., size and mass constraints.

(e) Determine payload volume, shape, and mass for the selected RRS sizes and configurations.

(f) Determine the degree to which user payload requirements are satisfied by each of the selected RRS, RM and related module sizes and configurations. Identify payload flexibilities, advantages, and disadvantages for each option. Particular attention shall be given to the payload electrical power and thermal control requirements.

(g) Examine the effect of various size/configuration options on vehicle refurbishment.

(h) Consider the effects of inheritance from other programs and possible spinoffs from this program to other programs on the size/configuration tradeoffs .

(i) Assess development risks for the selected sizes and configurations.

(j) Examine the effects of a low G reentry and landing on vehicle design performance.

Specific:

SRD Paragraph:

3.2.4.1 Atmospheric Reentry. The RRS shall be designed to accommodate the worst case reentry conditions for the range of orbits and potential recovery site(s). The reentry deceleration shall not exceed 15 g axial and TBD g lateral.

3.3.1 Structure Subsystem. The Structure Subsystem functions to provide attachment, mechanical support, and alignment of the RRS equipment and the PM through all environments of the mission without compromise to the functionality of the PM and RRS equipment.

3.3.1.1 Margin of Safety. A positive margin of safety (MS) shall be maintained in designing the RRS hardware:

$$MS = \frac{\text{Allowable Ultimate Load}}{\text{Qualification Load}}$$

The allowable ultimate load is the maximum load a structure can sustain without permanent deformation. The qualification load is 1.5 times maximum the expected flight load.

3.3.1.2 Refurbishment. The RRS structure shall be designed to permit easy removal/replacement of RRS subsystem components, and inspection and repair of the structure for damage during the refurbishment process.

3.3.1.3 RRS/PM Interface. The RRS shall be designed to provide a structural interface to secure the PM to the RRS. The PM shall not be used to carry any RRS loads. The PM mechanical interfaces are (TBD).

3.3.1.4 Launch Vehicle Adaptors. The RRS/launch vehicle adaptor(s) shall be designed to meet all the structural requirements imposed by the launch vehicle(s) and the respective launch environments.

1.3 Scope

This NASA Phase B study is intended to provide definition of the RRS concept. The study includes tradeoff studies, with the depth of analysis as appropriate, to clarify and document the viability of each approach. The RRS system and operations are developed to the degree necessary to provide a complete description of the designs and functional specifications. The RRS configuration trades described in this report were performed to ensure that the SAIC RRS design: 1) was capable of being aerodynamically stable, 2) sufficiently housed the required payload module, and 3) in general was adequate to perform the RRS mission.

2.0 STUDY APPROACH

2.1 Organization

The tradeoff analyses performed in Part 1 of the RRS Phase B study were organized to be accomplished in a series of related, but separate, tradeoff studies and system concept definitions. Therefore, the documentation described in these summary reports has been formatted to accommodate a compendium of analyses that are published in several separate documents. Because of the synergistic effect of one tradeoff study across the entire RRS system design, it is suggested that the reader review all summary reports to get a complete picture of the RRS design.

2.2 Document Format

Individual analyses and studies are not necessarily amenable to documentation in exactly the same topical arrangement; however, a general outline has been used where reasonable for all reports. The guideline for preparing the individual study sections in this and all summary reports is provided below:

- Purpose
- Groundrules and Assumptions
- Analysis Description
- Analysis Results
- Conclusions
- Recommendations

3.0 PURPOSE

The configuration, structure, and mass properties trade studies designed the RRV. The structural trades and analyses developed designs to provide support for the vehicle configuration selected. In addition, dynamic analyses of the extended vehicle were performed to determine the operational impacts of the configuration. In addition to meeting the design requirements, the RRS must be capable of reflight in 60 days. This drove the design in that the vehicle subsystems that required refurbishment had to be readily accessible.

4.0 GROUNDRULES AND ASSUMPTIONS

The baseline RRS system requirements for dispersion, reentry g loads, etc. are shown in (Table 4-1). In addition to these top-level requirements, the RRS configuration must:

a. Provide volume for the experiment and the Environmental Control and Life Support System (ECLSS). The payload volume was sized for containment of five plant cuvettes and their life support system. This required a 35-inch diameter payload volume and a 30-inch diameter ECLSS volume. Each section required 30 inches of length. The volume of the ECLSS and payload did not take into account expendables for the payload. This allowed derivation of the second requirement

b. Provide volume and support for payload expendables, which for the design case rodent module were: 49 pounds of oxygen, 25 pounds of air, and 133 pounds of water.

c. Allow access to the payload and or rodent module with minimal disassembly. This was to ensure that the 4-hour prelaunch and 2-hour after landing access requirements were met.

d. Provide volume for vehicle subsystems including power, propulsion, thermal, Guidance, Navigation and Control (GN&C), Telemetry Tracking and Command (TT&C) and recovery systems. The total volume requirements of all subsystems drives the overall vehicle size.

Table 4-1. Top Level RRS Requirements Affecting Shape Selection

REQUIREMENTS

- PARTIALLY REUSABLE
- RECOVERY DISPERSION
  - ±6 km Crossrange
  - ±30 km Downrange
- PRELAUNCH PAYLOAD ACCESS UP TO T-4 HOURS
- 15 g REENTRY LOAD
- NO EMERGENCY RETURN TIMELINE
- "OFF-THE-SHELF" TECHNOLOGY
- MINIMAL COST

GENERAL CONCLUSION

- NO INHERENT MISSION REQUIREMENT THAT DRIVES NEED FOR SOPHISTICATED SHAPES
- SAFETY AND COST BECOME PREDOMINANT ISSUES

The second set of major requirements for the SAIC design, maximizing the spin radius and meeting the stability margin, are conflicting. Maximizing the payload spin radius dictates locating more mass in the payload module in direct conflict with reentry stability criteria that wants mass to be located in the nose. The trade study work included packaging the payload and other subsystems to achieve the optimal mass balance. Requirements for the individual subsystems were related to their location and/or space view factor requirements and are covered in Section 6.

5.0 DESIGN OPTIONS AND DATA

The following sections describe the top-level design trades performed and derived data used to evolve the baseline configuration of the Reusable Reentry Vehicle (RRV). This analysis included an initial screening of potential reentry vehicle shapes for applicability to the RRS mission, followed by an initial estimate of vehicle mass properties that were used in more detailed aerodynamic, aerothermodynamic, and structural analysis.

5.1 Top-Level Shape Options

The overriding system requirement that affected the external configuration of the RRV was the requirement to reenter the earth's atmosphere for eventual recovery and reuse of the vehicle. In order to define the configuration capable of meeting this requirement, a top-level screening of potential candidate shapes was performed to determine which option best met mission requirements while at the same time satisfied safety requirements, and was relatively inexpensive. To analyze this situation, three classes of reentry vehicles were assessed: 1) high lift-over drag (L/D) shapes, 2) moderate L/D shapes and 3) ballistic shapes (no L/D).

High L/D shapes, typified by the Space Shuttle or lifting body type designs, use some type of wings to give the vehicle its high L/D. This type of design gives the vehicle appreciable cross-range and provides the capability to control reentry g levels somewhat. However, all these features are achieved at the expense of a fairly complex and expensive active control system. In the case of the Space Shuttle, a manned backup capability is also available to provide an added degree of safety in the system. In fact, all landings to date in the Shuttle program have involved a manual takeover for the terminal touchdown sequence.

Moderate L/D shapes have also been flown in past years, with the best examples being the Gemini and Apollo spacecraft. These vehicles were designed to provide some cross-range capability and some reentry g relief but did not use wings as do high L/D vehicles. The moderate L/D capability was achieved by incorporating a center of gravity offset from the center of pressure providing some lift capability. Such vehicles, as with high L/D vehicles, require active control systems but are generally not as complex and costly as high L/D systems.

As the name implies, ballistic shapes provide no L/D capability whatsoever and therefore provide no cross-range capability. Reentry g levels are determined strictly by the reentry profile provided by the de-orbit burn. This type of vehicle has been flown in the Discoverer and Mercury Programs and used on ballistic missile reentry vehicles. Since such shapes are truly ballistic, no active control system is required for reentry. Ballistic vehicles are, thus, less costly than other types of vehicles.

Figure 5-1 reviews pros and cons of each of the shapes discussed above. When comparing the features of each reentry shape against the requirements of the RRS mission, no reason could be found to justify using the more complex and costly shapes. No inherent cross-range requirements were specifically stated in the System Requirements Document other than the overall safety issues

and dispersion requirements associated with a land recovery. It was felt that these safety issues could be adequately addressed using a ballistic shape coupled with a very accurate de-orbit guidance and propulsion system. The maximum reentry g level of 15 g stated in the SRD could also be achieved with considerable margin for all missions without the use of lifting shapes. As mentioned previously, a ballistic shape also negated the need for an active guidance system, thus reducing the overall cost and complexity of the vehicle. For these reasons, a ballistic shape was selected for refinement in subsequent stages of the design study.

HIGH L/D	MODERATE L/D	NO L/D
GOOD CROSS RANGE	SLIGHT CROSS RANGE	NO CROSS RANGE
LOW REENTRY G'S	LOW/MODERATE REENTRY G'S	MODERATE REENTRY G'S
COMPLEX ACTIVE CONTROL SYSTEM	ACTIVE CONTROL SYSTEM	BALLISTIC
HIGH COST	MODERATE COST	LOWER COST
FLIGHT PROVEN	FLIGHT PROVEN	FLIGHT PROVEN

TOR42B/19

Figure 5-1. Top-Level RRS Shape Options

5.2 Initial RRV Mass Properties

To investigate and refine the ballistic shape required for RRS aerodynamic analysis, a spreadsheet program entitled MASSMASTER was developed to provide mass properties information on the RRV. The program provided center of gravity (CG) information as well as moments of inertia data that were used in aerodynamic, structural, and propulsion analyses. The program itself treated the various components of the RRV as point masses in the Z or length direction. The tip of the nose (spherical section) was defined as the the zero point for the coordinate system. Moments of inertia about the Z axis were estimated assuming a radius for the components from the axis, and assuming a cylindrical distribution of the component's mass.

The program was setup for the two configurations of the SAIC design. The first analyzed the stowed configuration, while the second analyzed the extended, or deployed, configuration. In this manner, the spin radius and launch/de-orbit mass properties could be reviewed quickly. De-orbit (or reentry) mass properties are important for determination of the stability margin for aerodynamic analysis. These properties were based on the assumption of a return to land at T+1 day with all propellant consumed prior to atmospheric penetration. This was considered a worst case condition, since during a nominal 60-day mission mass transfer (carbon dioxide and rat waste) would move the vehicle CG towards the nose of the vehicle, thus providing greater stability.

6.0 AERODYNAMIC ANALYSIS

The use of conventional, flight-proven, sphere-cone ballistic reentry vehicle shapes has been emphasized in the tradeoff studies from which the baseline RRV has evolved. In concert with vehicle packaging and design studies, analyses were performed to evaluate the aerodynamic stability of candidate RRV configurations. A design criterion was established that the RRV provide a minimum aerodynamic static margin equal to 10% of its vehicle length throughout the reentry trajectory. (The static margin is the distance between the vehicle center of gravity location and its aerodynamic center of pressure location, the difference being nondimensionalized by vehicle length. A vehicle is aerodynamically stable when the center of pressure is aft of the center of gravity.) The 10% static margin design criterion was selected based on SAIC's considerable design experience with other successful ballistic reentry and planetary entry vehicle systems, and should ensure that the RRV will have stable, repeatable aerodynamic reentry flight performance with very low aerodynamic-induced dispersion.

In the process of evolving the current baseline, the stability of candidate RRV concepts was assessed over a full range of reentry trajectory Mach numbers from hypersonic ($M_\infty > 20$) to subsonic ($M_\infty \approx 0.6$). Initial screening was performed at Mach 20, and then at a lower supersonic condition (typically $M_\infty = 3.5$). Results and trends for vehicle center of pressure at Mach 20, as a function of cone angle (θc) and bluntness ratio (R_N/R_B), are presented in Figure 6-1. Figure 6-1 also indicates the center of pressure for some of the candidate designs that are discussed later in this section. For candidate configurations that met the stability margin design criterion at the aforementioned Mach numbers, stability was evaluated at the low-supersonic, transonic, and high subsonic conditions that the RRV would encounter prior to initiation of the recovery sequence.

6.1 Aerodynamic Stability

The RRV aerodynamic stability characteristics at supersonic and hypersonic flight conditions were evaluated using accurate, validated flow field prediction methodologies that SAIC personnel have developed and applied previously to strategic RRV designs for the Air Force and to planetary entry probe designs, such as Pioneer Venus, for NASA. For purposes of reentry vehicle aerodynamic design and analyses, the use of inviscid Euler codes represent a proven, accurate, and effective methodology. In particular, the 3-D Shock and Pressure (3DSAP) inviscid Euler code developed by SAIC personnel provides a very efficient and useful capability, and hence, was applied in this RRV analysis. For viscous aerodynamic calculations, as well as aerothermal calculations, the 3DSAP code has been coupled to an integral boundary layer code and to a trajectory code. This SAIC integrated aero/aerothermal/trajectory capability has been used (as will be discussed later) to predict RRV drag, g loads, and aerothermal heating throughout reentry.

For many reentry vehicle analyses, the environment of primary interest is the lower altitude flight regime ($h < 50$ km) where peak aerodynamic loads and heating are experienced. In this region, the vehicle shock layer can often be modeled as primarily inviscid, with a thin boundary layer adjacent to the body surface. Consequently, inviscid flow field techniques are widely used to predict the predominant aerodynamic forces and moments (e.g., normal force, pitching moment, inviscid contribution to axial force) as well as to provide edge conditions for viscous boundary layer calculations. Finite-difference solutions of the inviscid equations have been used to obtain accurate flow field predictions for reentry vehicles in this flight regime for almost two decades.

The calculation of a complete inviscid flow field on a reentry vehicle requires two different solution methods. On the blunt nosetip where the flow is subsonic, the steady inviscid equations are elliptic, and the steady flow solution is obtained as the asymptotic limit of an unsteady solution starting from an assumed flow field about the body of interest. Downstream of the nosetip, the

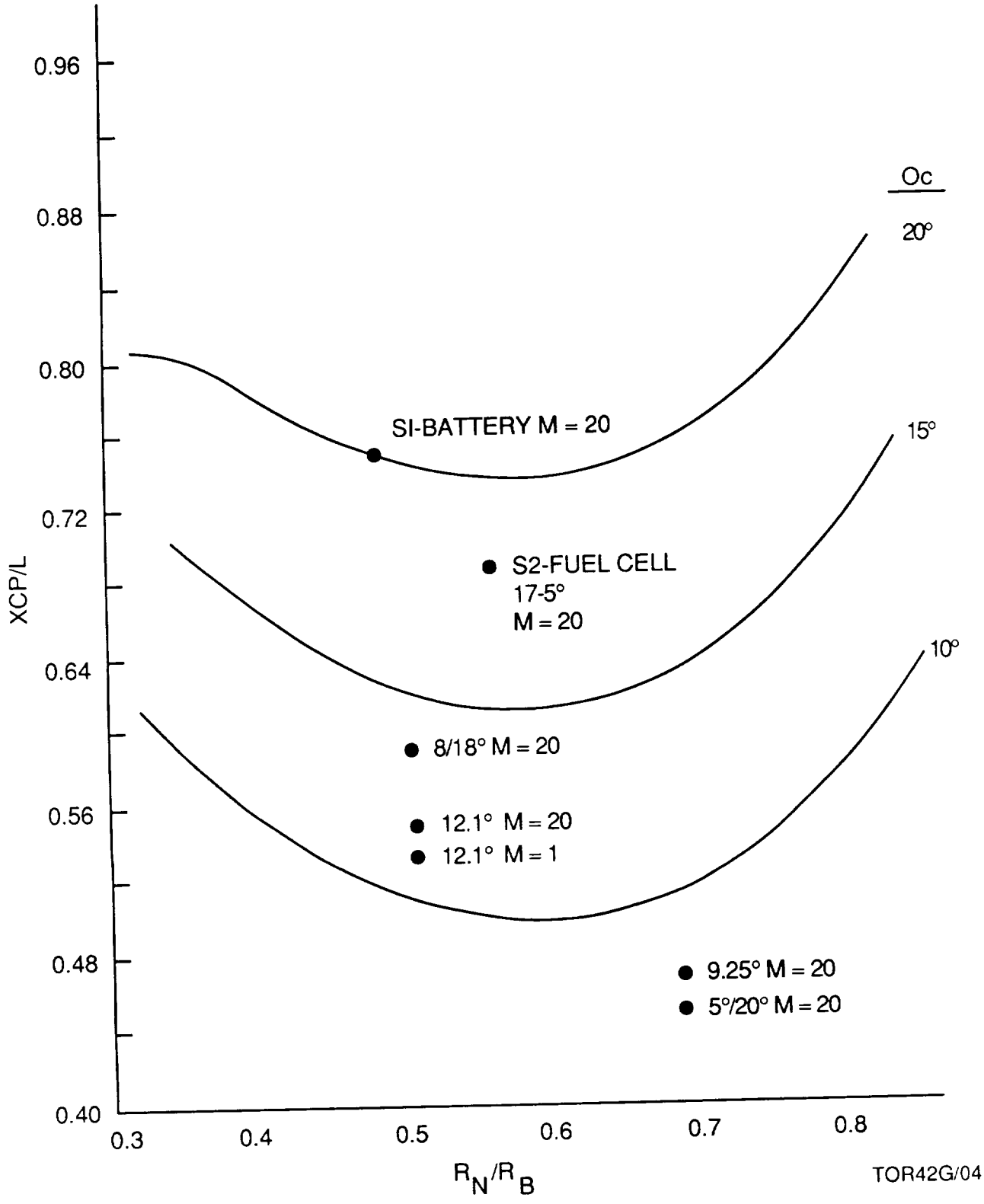

Figure 6-1. Center of Pressure vs. Cone Angle and Bluntness Ratio

shock layer flow is supersonic, and the steady flow equations are hyperbolic, allowing the use of a forward marching (in space) integration procedure, starting from initial data obtained from the nosetip solution.

Existing finite-difference inviscid flow field codes have demonstrated capabilities for making accurate aerodynamic predictions very efficiently, allowing their routine use in reentry vehicle design and analysis efforts. Despite this efficiency, however, there are problems for which current inviscid flow field calculations are too time-consuming, limiting the amount of useful information that can be generated with available computer resources.

Approximate inviscid flow field prediction methods such as the 3DSAP code have been developed to reduce the computer time requirements for reentry aerodynamics simulations and still retain high accuracy for zero-lift and small angle-of-attack predictions of forces and moments. Since finite-difference nosetip flow field solutions for nonspherical shapes can use 80 to 90% of the total computer time required for a complete inviscid shock layer calculation (nosetip and afterbody), the 3DSAP code achieves its efficiency primarily by using an approximate nosetip solution method. In this procedure, nosetip surface pressures are assigned using a correlation and the bow shock shape is determined using a mass balance iteration, assuming the functional forms of the flow properties across the shock layer. On the afterbody, 3DSAP obtains a finite-difference solution of the inviscid flow equations. For greater efficiency, these calculations are performed using only three circumferential planes in the computational grid (the wind, side, and lee planes) and assuming the functional forms of the circumferential variations of the flow properties.

The 3DSAP calculation procedure has been extensively validated versus ground and flight test data. The code has been found to be accurate for angles of attack up to approximately 15 degrees for a broad range of typical reentry vehicle configurations at hypersonic and supersonic velocities (to below Mach 3); and, hence, it was an appropriate choice for this analysis.

Over the subsonic, transonic, and low supersonic portions of the reentry trajectory, RRV stability was evaluated primarily based on available wind tunnel data for similar configuration classes. A reasonably satisfactory database exists for this purpose. Although SAIC has sophisticated computational fluid dynamic (CFD) techniques, such as the time-dependent Euler codes and Navier-Stokes codes, that could be applied at these lower speed regimes, the use of such costly computer-intensive techniques was not considered appropriate for RRV tradeoff and preliminary design analyses. This analysis used an integral aero/aerothermal/trajectory capability which features an efficient Euler inviscid flow field technique (3DSAP) to calculate the vehicle

flow field, and an integral boundary layer technique to determine viscous and aerothermal effects. A boundary layer transition altitude of 80,000 feet was assumed for all reentry trajectories.

6.2 Aerothermodynamics

The aerothermal portion of the 3DSAP code utilized the flow field solution to define the local boundary layer edge properties and local surface pressures that serve as the boundary conditions for the boundary layer solution. An approximate procedure for modeling the transient heating and material response of ablating thermal protection systems is included using a heat balance integral (HBI) methodology.

Some of the capabilities of the boundary layer code include:

- The ability to treat equilibrium air thermodynamics in a manner consistent with the 3DSAP inviscid code
- The ability to automatically determine the wall temperature and mass addition rates for ablation model heat shields using transient or steady state ablation model options
- The ability to treat laminar, transitional, or fully turbulent flows

The code is a solution procedure for the boundary layer integral momentum and energy equations in a streamline-body normal coordinate system over a general three-dimensional body. Laminar, transitional, or turbulent flows can be treated, and the procedure accounts for compressibility, real gas effects, and surface ablation.

Closure of the set of integral equations is accomplished by specifying the local shape factor, the recovery factor, the Stanton number, and the friction coefficient as functions of the momentum and energy thickness Reynolds number. These basic "laws" are modified to account for the effects of surface roughness, transpiration, acceleration, and compressibility by influence coefficients which are multiplicative factors on the local Stanton number and friction laws. The numerical solution procedure is an implicit finite difference scheme.

There are five flow phenomena subroutines built into the boundary layer code that provide solutions to: 1) flows with pressure gradients, 2) transpiration cooling effects, 3) characteristics within the boundary layer, 4) surface roughness effects, and 5) transition and transitional flow regime models. In each of these flow regimes, the code provides solutions based on recent work performed in the U.S. aerospace community that provides accurate solutions in those areas where

the methodologies are applicable. For example, mass transfer effects on wall shear and viscous flow properties are modeled by adaptation of film theory. Surface temperature and ablation modeling is included in both the steady state form (i.e., no transient conduction in the solid) and also with a transient response capability. The wall response modeling built into the code enables solutions to be obtained efficiently where the wall boundary conditions, in terms of local temperature and mass transfer rate, are determined as a part of the solution, and where the local viscous properties include these effects as well. Surface roughness effects on heating are modeled from ground test data results and correlations.

Overall, this integrated aero/aerothermal/trajectory solution methodology provides a reliable method for engineering prediction of aerodynamic loads and surface heating on space reentry vehicles such as the RRV while being efficient enough (through the use of an integral boundary layer methodology) for routine use in both vehicle design and analysis.

6.3 Analysis Results

As discussed in Section 5.1, vehicle reentry and landing requirements, coupled with the desire to minimize cost and maximize public safety, drove the design of the RRV to a ballistic shape. This negated the need for an active control system requirement during the reentry. Given a ballistic shape as a guideline, further design evolution used the methodology outlined in Figure 6-2.

The SAIC RRV configuration evolved as shown in Figure 6-3. The design work started with the AMES study 10-degree sphere cone or Discoverer shape. The volume of this shape was insufficient to house the ECLSS and related systems for the 18-rodent/60-day requirement and, thus, the first design iteration was a shape from the proposal (sphere cone with flare). An increased stability margin was achieved with the flared end of the vehicle; however, the shape was subsequently modified due to the very high localized heating at the flare. The flared configuration also presented analysis difficulties associated with fully understanding the vehicle's dynamics through all phases of reentry. Thus, in order to achieve greater stability and increased volume while still maintaining a conventional shape, the third 12.1-degree sphere cone baseline was developed. Increases in the power system volume requirements caused this design to be modified as well, leading to the last two configurations shown in Figure 6-3 to be carried forward for further study. The two designs both incorporated 20-degree sphere cone designs. The difference between the two designs was the fuel cell power system that required a 5-inch increase in diameter to contain the additional reactant tankage required for the fuel cell power system

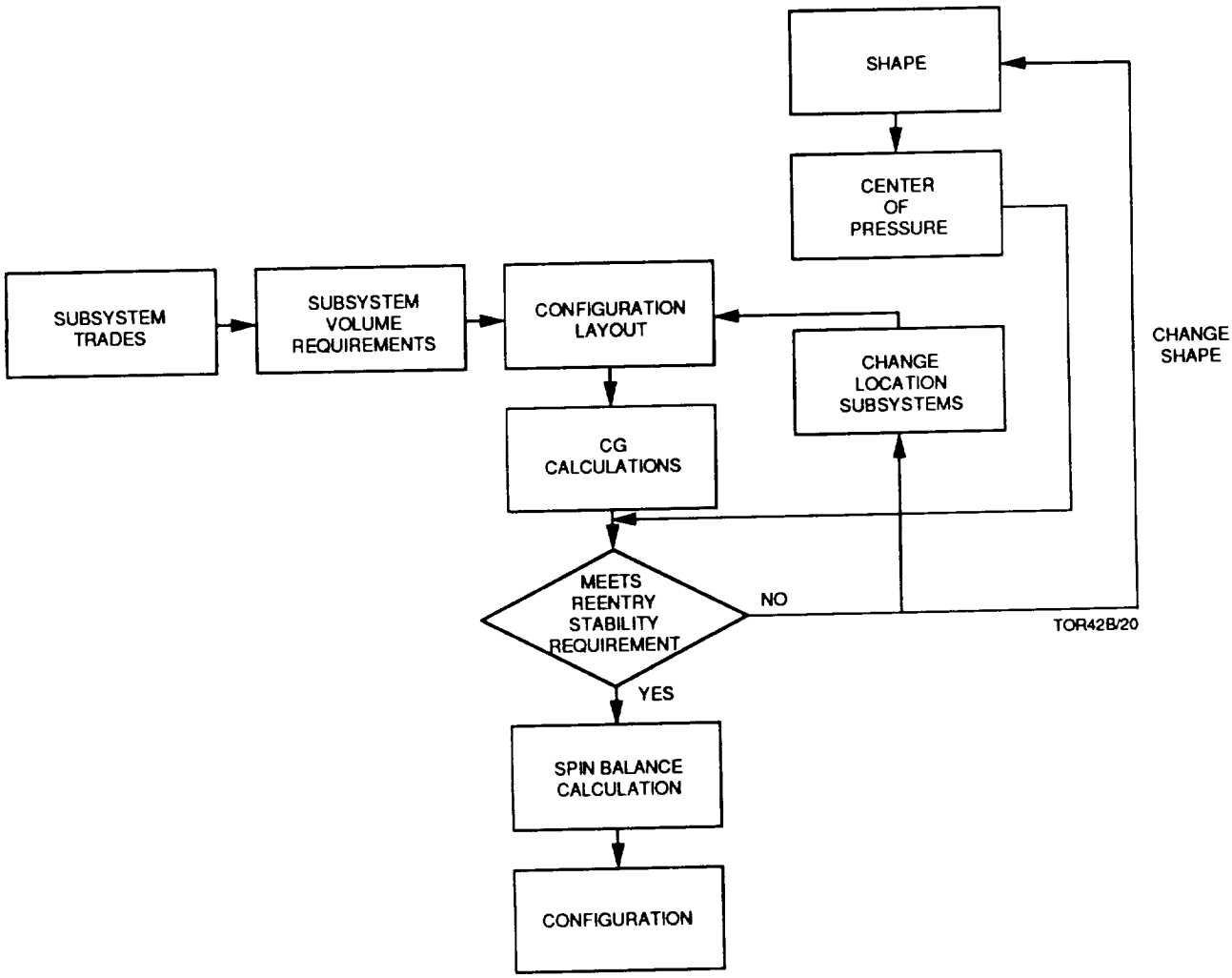

Figure 6-2. Configuration Evolution Methodology

A baseline RRV configuration has evolved to a configuration that accommodates the efficient packaging of all RRS payloads, support systems, and satellite subsystems, while at the same ensuring stable aerodynamic flight performance throughout the reentry trajectory. The baseline vehicle is a 95.3-inch diameter, 20-degree sphere-cone having a bluntness ratio of 0.48 and a total main body (does not include antenna and thruster protrusion) length of 87.6 inches.

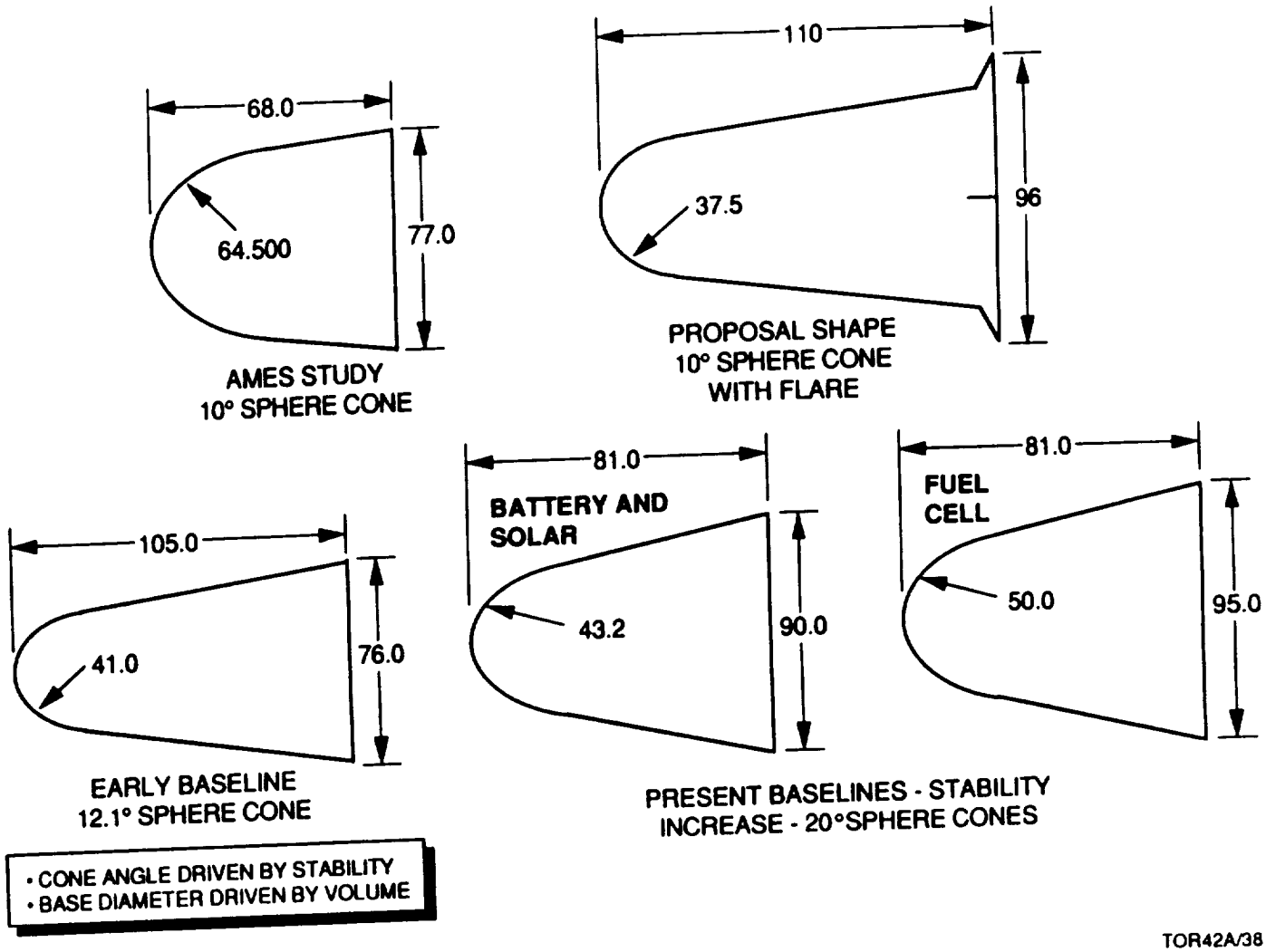

Figure 6-3. Configuration Evolution

An RRV reentry analysis was also performed to determine the axial deceleration g loads and stagnation point heating on the baseline RRV configuration during reentry from 350-km and 900-km circular orbits (corresponding to Design References Mission (DRM) 1, 2, and 3). The analysis was performed assuming a vehicle weight at reentry of 3000 pounds. Calculations for each of the DRM reentry trajectories was initiated at 400,000 feet altitude, and the resulting plots of g load and heating histories are referenced to this 400,000 feet condition as the starting time (t=0). Figure 6-4 summarizes the peak g loads for the various reentry trajectories. Figure 6-5 presents the time histories of the stagnation point heating, respectively, for these DRM cases. It can be seen from the figures that the maximum axial deceleration g load ranges from a low value of 8.3 (for DRM 1 with delta-V = 100 m/s) to as high as 16.8 (for DRM 3 with delta-V = 350 m/s). For a given DRM, the maximum g load can be tailored (to some extent) by the choice of the de-orbit delta-V, which in turn controls the reentry flight path angle. The higher the value of delta-V, the steeper the reentry flight path, and the higher the g loads and heat flux to the vehicle.

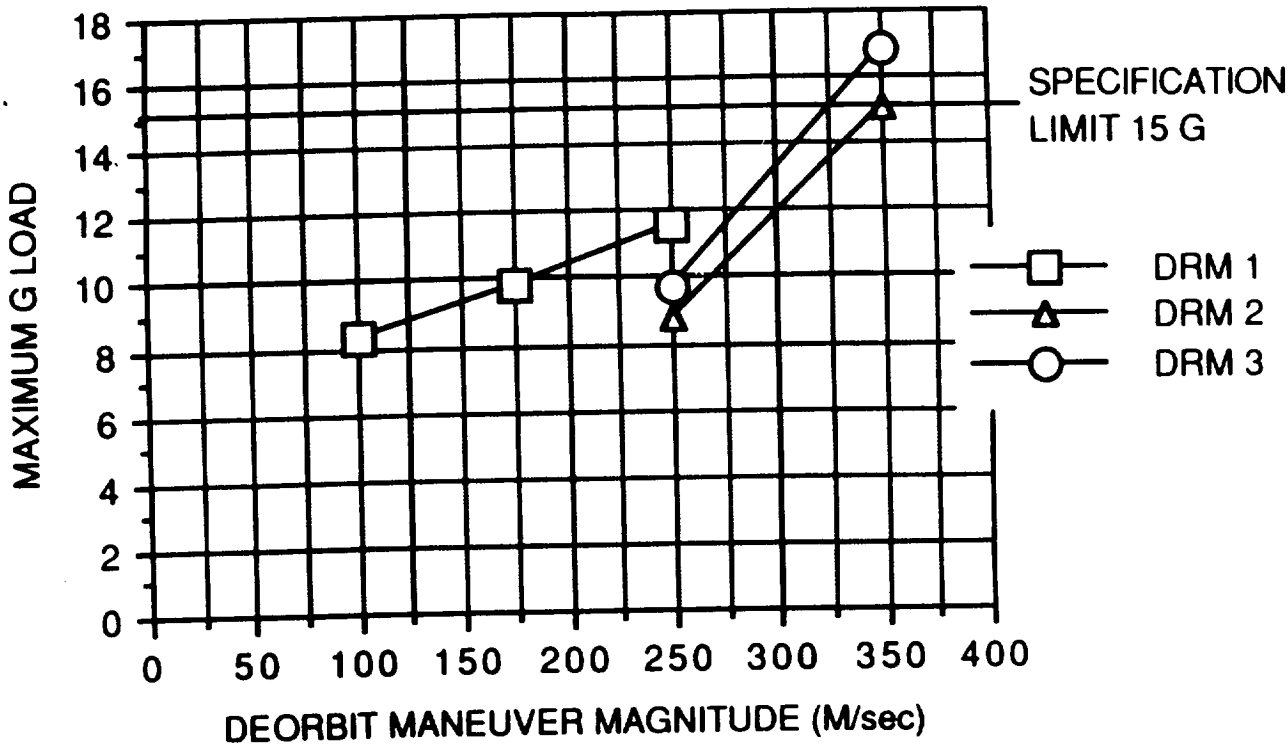

- Single Burn Deorbit
- Multiple Burns Can be Performed to Achieve 8g Limit (DRM2 + 3)

Figure 6-4. Reentry Loads Versus De-orbit Maneuver

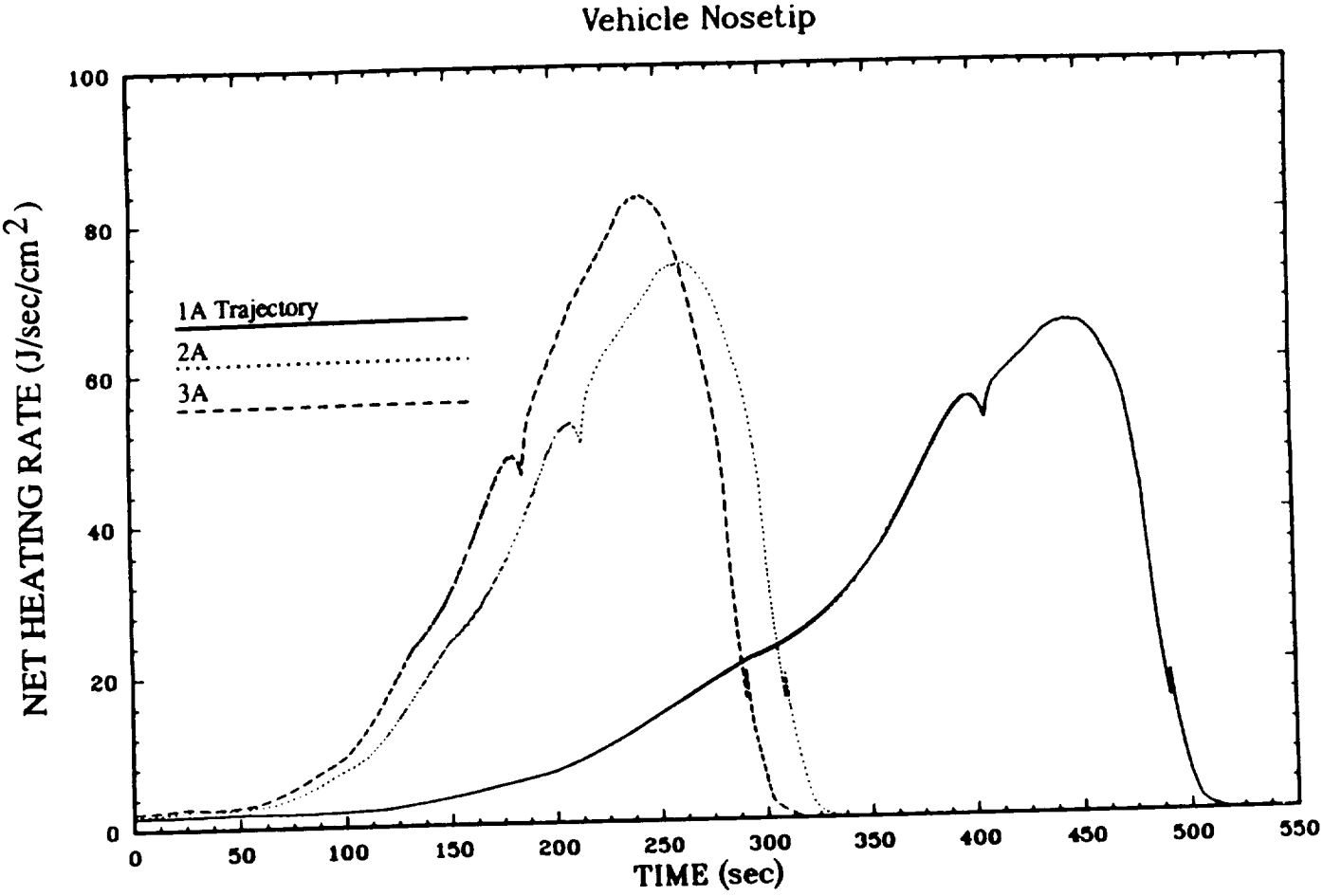

Figure 6-5. Results—Examples of Net Heating Rates Predicted by SLAPEM

7.0 STRUCTURAL ANALYSIS

7.1 Layout of Vehicle Subsystems

The following sections describe the vehicle subsystem layouts used to set the stage for the structural analysis. The vehicle subsystem layout was driven by the goal to obtain as equal a mass distribution between the main and deployed module as possible while at the same time allowing adequate static margins for reentry.

7.1.1 Payload

The Payload Module and ECLSS are located in the main module. This is required so that during artificial g missions, the major acceleration forces are in the same direction through all phases of the flight. The Payload Module, ECLSS, and assorted data command and power systems constitute almost one-third of the vehicle dry mass. Thus, to achieve a large spin radius for artificial g missions (spun), other subsystems need to be located in the deployed module. The vehicle mass balance must be forward enough to ensure reentry stability as described in Section 6.3.

7.1.2 Propulsion

The propulsion system was located at the rear of the vehicle. This location served two important functions. During on-orbit artificial gravity operations, it increased the spin radius of the payload module by having a large countermass at the deployed end of the vehicle. De-orbit maneuvers required for atmospheric entry consume the propellant in the tanks shifting the CG forward which is beneficial in maintaining an adequate static margin for atmospheric entry.

An early configuration-related trade performed for the propulsion subsystem (and described in detail in the Propulsion Summary Report) was the de-orbit thruster firing direction and the option of having a jettisonable propulsion module. The design postulated in the SAIC proposal incorporated a jettisonable thruster module. The propulsion module was optimized to interface with the launch vehicle cradle and configured to provide de-orbit thrust in the same direction as all other accelerations encountered during a mission. Safety and cost issues warranted this design to be reevaluated early in the trade study. The safety issue was one of ensuring complete burnup of the module (and hence no debris) over populated areas. The cost associated with replacing the propulsion module for each flight ($2 to $4 million) was not considered trivial. Thus, design options that retained the propulsion module and maintained the acceleration direction in a single direction were investigated. Three possible solutions were evaluated. The first had holes in the heat shield that allowed the thrusters to fire towards the nose of the vehicle.

The desire to maintain a uniform g-load direction on the RRS payloads from launch through recovery led to the consideration of forward firing thrusters for the de-orbit engines. One version of this concept would have required a series of holes in the RRV frustum heat shield, through which the thrusters could fire. An obvious concern existed about the thermal survivability and viability of unprotected thruster nozzle designs that would have to be exposed to the hostile aerothermal reentry environment.

To resolve this issue, an analysis was performed to quantify the heating environments and temperatures to the forward firing thrusters during reentry and thereby determine the feasibility of the concept. The nozzle exit plane of each forward firing thruster was assumed to be flush with the surrounding heat shield surface. The basic aerodynamic flow field and heat flux characteristics over the vehicle in the vicinity of the nozzle opening were computed using the same aero/aerothermal/trajectory techniques described previously. The nozzle opening was modeled as an open cavity, and engineering methodologies plus data were applied to assess the heating augmentation that could occur inside the nozzle cavity.

Local heating augmentation factors of between 1.5 and 2.0 were calculated for the downstream lip of the engine nozzle and were used in determining the temperature response of the nozzle material. A 0.10-inch thick Columbian nozzle was considered, and the resultant heat flux temperature was calculated. Unacceptably high temperatures (in excess of 3000° R) were predicted to occur near the downstream edge of the nozzle (where the heating augmentation is greatest). Increasing the nozzle wall thickness by reasonable amounts did not appreciably reduce the surface temperatures. Therefore, it was concluded that these temperatures precluded the safe use of the forward firing thruster through the heat shield, and hence this concept was eliminated as a viable RRS candidate.

The second design solution incorporated the de-orbit thrusters on deployable booms. The booms would extend for engine firing and retract prior to atmospheric entry. This concept was rejected almost immediately on the basis of complexity and the unknown safety impact if one boom failed to retract.

The third concept had the de-orbit thrusters mounted in the deployed module but firing forward. The idea was the astromasts would retract approximately 90 feet out of the total 100 before the de-orbit burn. After the burn, the deployed module would be retracted completely which would shield the nozzles under the heat shield for reentry. This shortened configuration would be much stiffer and capable of handling the side loads produced by the reentry burn. The side loads are from combustion instability and thruster-to-thruster variation in design thrust. This concept had the advantages of no additional hardware but was subsequently rejected for safety reasons. If the astromast failed to retract after burn completion, a debris hazard would be present similar to the jettisonable propulsion module discussed earlier.

As described above, none of the designs investigated offered a simple inexpensive way to provide the de-orbit acceleration in the direction desired. Since this feature was not a requirement for the RRS program, but was a beneficial feature of the initial SAIC design, discussions were initiated with the life science personnel on the relative degree of importance of the design feature compared to overall mission requirements and goals. The response was the feature was not critical and could be discarded with no adverse payload implications if it unnecessarily complicated the engineering design. For this reason, it was decided to fire the de-orbit thrusters in a more conventional fashion towards the rear of the vehicle. After the burn, the vehicle would reorient itself nose first for reentry. This type of design simplified the propulsion system integration into the vehicle and offered the lowest risk approach.

7.1.3 Power

The power system was the major driver in determining final vehicle size and volume. For this reason, three independent design configurations were postulated at the beginning of this trade study to evaluate how the power system affected RRV configuration. The power system trades are discussed in detail in the Power System Summary Report and are summarized here as they affected configuration. Power system component layouts were based on the CG requirements of the vehicle and design requirements of the system.

Battery systems offered the most flexibility in terms of internal component placement. Battery cell strings (providing 28 volts) were incorporated such that placement of strings was modular to facilitate balancing the vehicle for artificial gravity spin balance and reentry stability requirements. The large mass associated with battery systems gave this system the largest payload spin radius of any of the designs, which is a plus for artificial gravity missions.

Fuel cell systems investigated for this study incorporated the fuel cell and the reactant tankage in the main module of the vehicle. The tank volume for a 60-day mission required a 5-inch increase of the vehicle diameter to incorporate the additional tankage.

The solar power design required minimal mass and volume compared to the battery and fuel cell versions. For this configuration, the outer circumference of the deployed module was covered with solar cells. During the launch and reentry portions of the flight, the solar cells are protected under the heat shield. The arrays are then exposed as the two modules of the RRV deploy for the baseline orbital configuration.

Fuel cell, battery, and solar panel designs are depicted in Figures 7-1 through 7-3.

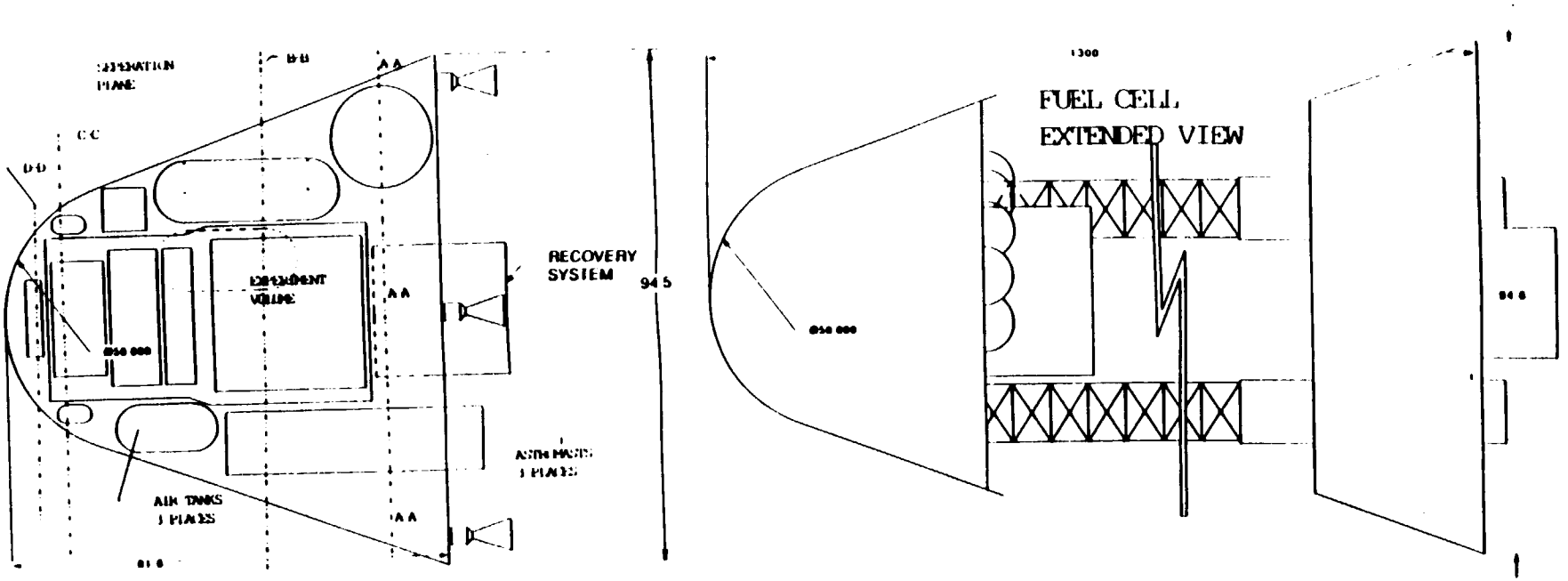

- SPLIT HEAT SHIELD
- VEHICLE LARGER FOR TANKAGE

Figure 7-1. Fuel Cell Design

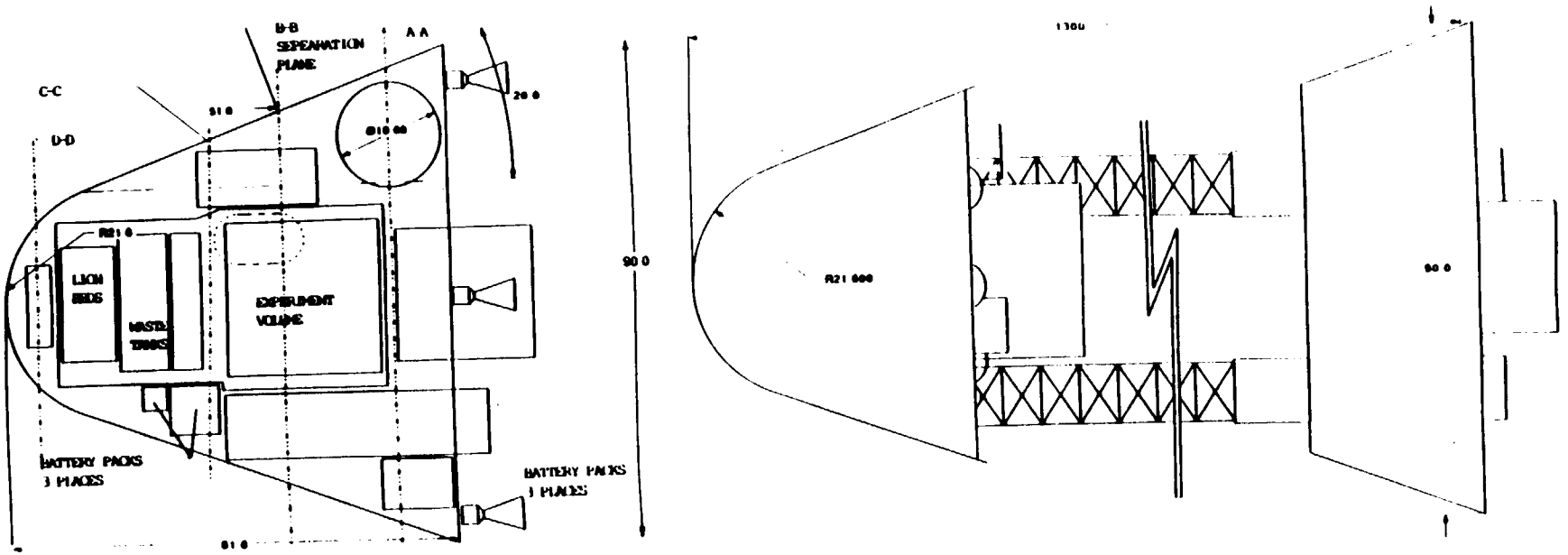

- $Li/(CF)_X$ BATTERY POWER
- SPLIT HEAT SHIELD
- BASELINE FROM PREVIOUS REVIEW

Figure 7-2. Battery Design

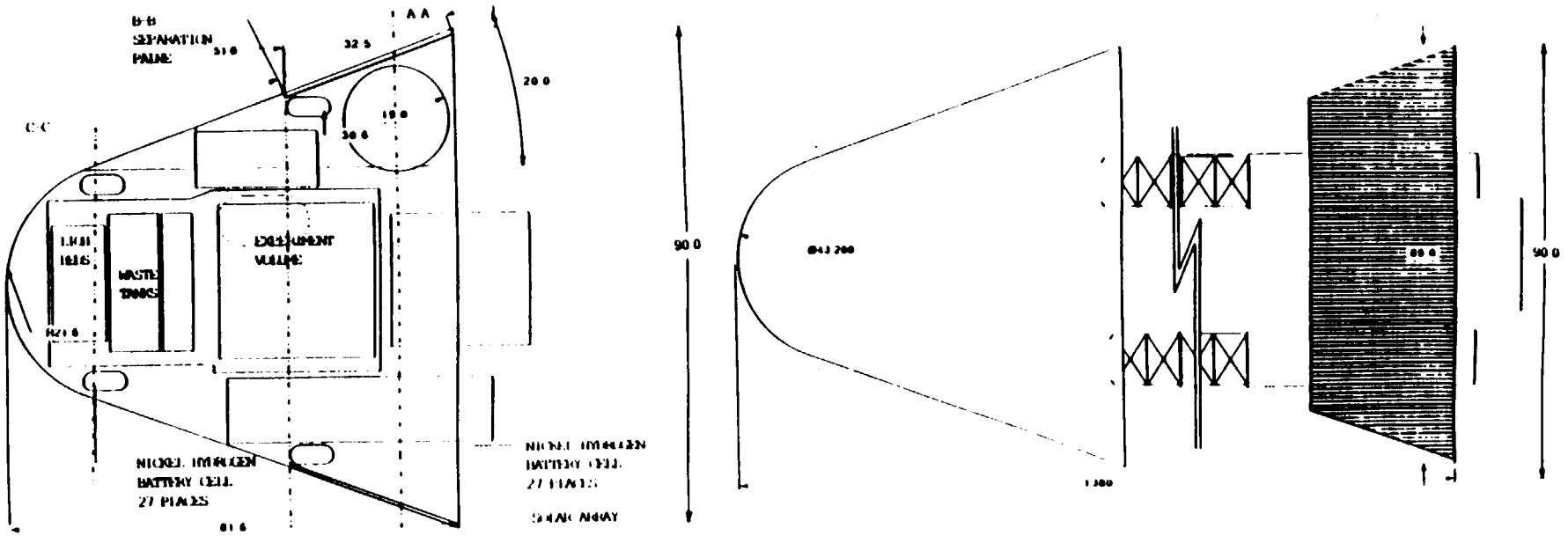

- HEAT SHIELD CONTINUOUS
- SOLAR ARRAY ON EXTENDED MODULE

Figure 7-3. Solar Power Design

7.1.4 Thermal

The battery and fuel cell powered versions discussed above incorporated a split heat shield design that included a thermal radiator that was integral to the top half of the payload module. The solar powered version, which had a continuous heat shield, had the thermal radiator located beneath the reentry thermal protection material due to limited aft radiation view factors for the extended heat shield design. The payload module thermal radiator offered the advantages of fast response time and could be covered with quartz mirrors making it highly efficient and capable of rejecting large quantities of heat. The downside of this concept was the payload module was not an integral part of the vehicle, making the total system less modular and increasing the interface complexities. The solar power design, which was eventually baselined, radiated through the heat shield. Though this concept was less efficient than the other, it was feasible for the solar version due to the large surface area available. In addition, this concept did not impact the payload module design.

7.1.5 Electronics

Most vehicle electronics, including GN&C, TT&C and the main vehicle computer were located in the deployed module. This facilitated system operation and kept cable connections between the two modules to a minimum.

7.1.6 Terminal Recovery System

The terminal recovery, or parachute, system is located above the payload experiment module with attachments to the deployed module. This is the only piece of hardware that needs to be removed to access the experiment module. This location provided attachment to the RRS main structure along the aft ring described below.

7.2 Main Structure

This section describes the methodology and data used to develop a structural design for the primary structural elements of the RRS. The resulting design is substantiated by sufficient design analysis detail to provide structural weights within 10% accuracy.

7.2.1 Loads

The primary load conditions considered for design purposes were divided into three major categories: Prelaunch and Launch, On-Orbit Operation, and Recovery. By far the most important condition for overall design of the RRS structure is that of reentry, because it produces a maximum worst case 15.1 g of axial acceleration. In contrast, the axial load during launch only reaches 5.8 g, and the on-orbit loads are negligible by comparison.

7.2.2 Design Criteria

To ensure that uncertainties in the load environment and/or analysis methods will not jeopardize the design, an ultimate factor of safety of 1.5 for all loads was used for design analysis. Also, since yielding is unacceptable, a yield factor of safety of 1.1 was used.

7.2.3 Configuration Structural Design

The RRS utilizes conventional, lightweight aerospace design approaches to carry the structural and thermal loads during ascent, on-orbit operation, reentry and landing. To establish a baseline design, 6061-T6 aluminum alloy is used for virtually all of the RRS structure. This material was chosen for the same reasons it was selected in the Phase A study (Reference 1): high strength, corrosion resistance and weldability.

The principal load carrying elements of the RRS structure are the conical sandwich, ring-stiffened heat shield, the radial shear webs, the truss support system, and the primary and secondary thrust beams at the aft end of the structure. Other important elements are the nose cap, aft cover, equipment supports, shear web longerons, and the forward payload attachment ring. Figure 7-4 depicts the top view of the major RRS elements, and Figure 7-5 shows the overall arrangement of the primary and secondary thrust beams.

The conical heat shield was chosen to be a ring stiffened sandwich shell to carry the axial and pressure loads during reentry. This type of structure is highly conventional for this type of application. The ablative material used for heat dissipation was assumed to keep the 6061-T6 aluminum material to less than 350° F; however, the ablative material's load-carrying contribution was ignored.

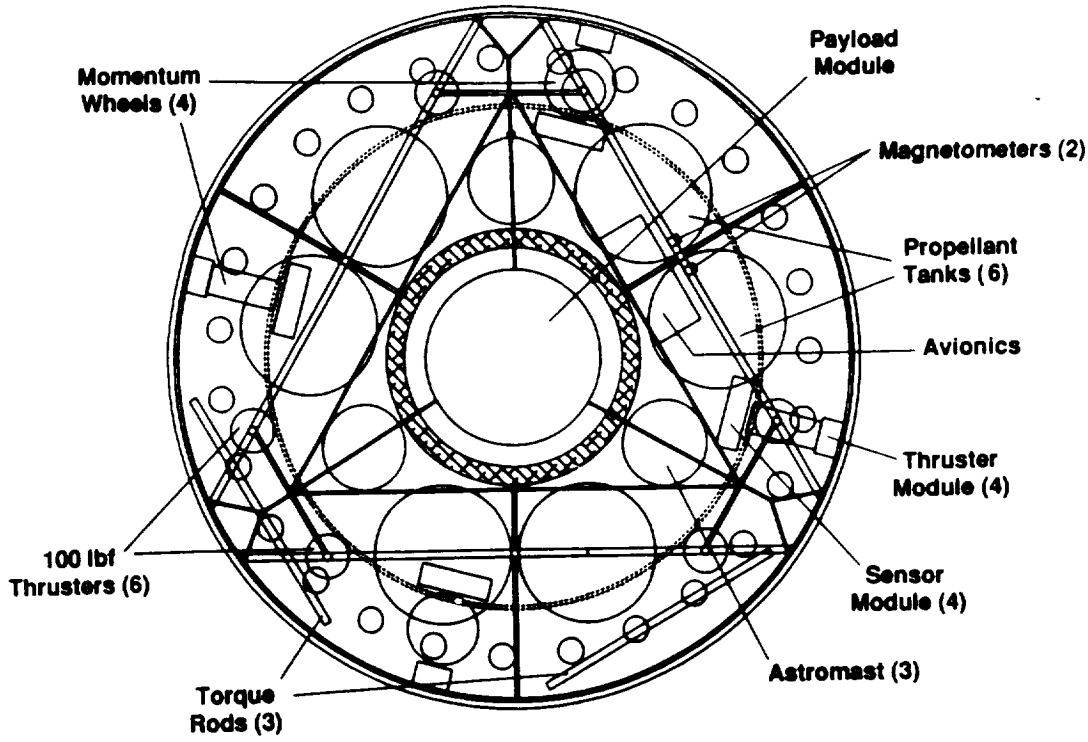

Figure 7-4. RRS Top View

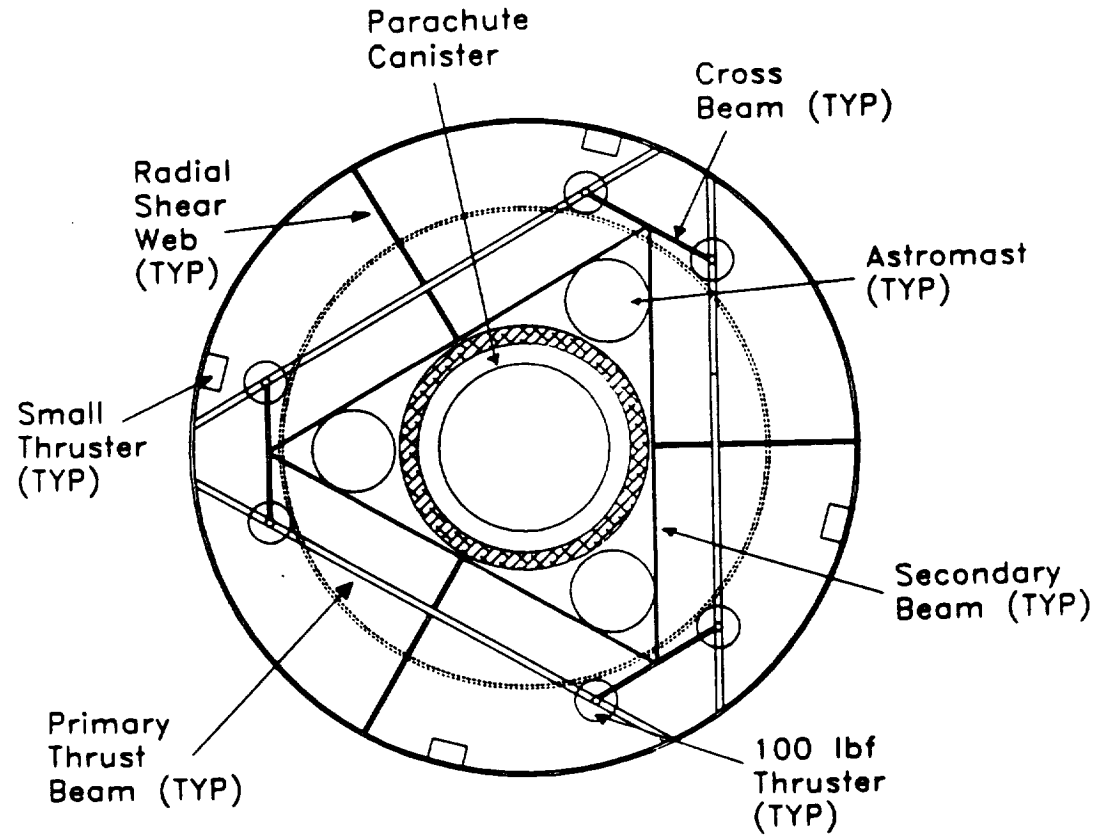

Figure 7-5. Arrangement of Primary and Secondary Thrust Beams

The three radial shear webs and the truss support system comprise the primary internal structural load-carrying capability for payload support under axial loading. However, for additional security, the payload canister also receives axial support from three payload support members which, on one end, attach at 120-degree spaced locations on the canister ledge and, on the other end, attach to similar locations on the forward support ring at the cone/sphere junction of the external shell. The radial shear webs are conservatively sized to provide all of the axial load restraint whereas, in actuality, the payload support members and the truss support tubes do provide some additional support. The truss support system, together with the forward payload attachment ring, can easily resist any torsional loads that may develop. Lateral loads will be carried by a combination of the radial shear webs and their stiffeners, the truss support system, and the forward payload attach ring.

The primary and secondary thrust beams at the aft end of the RRS provide several load-carrying functions. As already noted, during ascent, the entire RRS is supported by these beams being attached at their base to a surrounding cylindrical shell which is later jettisoned. The ends of these beams are attached to an aft ring, which, in turn, is attached to primary thrust longerons; these longerons are tapered and attached meridionally to the conical heat shield substructure. The primary thrust beams also support the cross beams, which, in turn, are attached to the secondary beams to form an efficient, stable structure. Altogether, this beam system provides support for the six primary (100 pound) thrusters and the propellant tanks, and lateral support for the payload canister and the Astromasts. Finally, the base of the primary thrust support beam structure is designed to carry the major chute opening loads during parachute deployment. The beam system carries virtually all of the loading arising at the aft end; therefore, the aft cover is a lightweight structure that primarily functions to provide some thermal protection and to seal off the RRS interior from the external environment. However, pressure or inertial loads on the aft cover are expected to be minimal.

The nose cap is designed to impact the ground upon landing, and is therefore expendable. Initially, it was also considered to be a sandwich structure, but sizing analyses for reentry pressures showed that a monocoque spherical shell would suffice. Landing shock will be managed by crushable aluminum honeycomb behind the monocoque shell. The current design is capable of a 10 g landing with an impact velocity of about 15 ft/sec.

A variety of approaches are used to support the internal equipment such as batteries, propulsion tanks, batteries, GN&C equipment, and Astromasts. Generally, with the collection of internal structure such as the primary rings, radial shear webs, truss support structure, and the aft

thrust beams, no problems are encountered in finding a sufficient number of stable nodal points from which to attach ancillary equipment.

7.3 Structural Design Analysis

This section briefly describes the methodology and procedures used to develop the current designs for the primary elements of the structural subsystem. Topics treated are the conical shell, radial shear webs, truss system, aft structure, equipment supports, nose cap, and Astromast dynamics.

Before beginning the design analysis discussion, it is worth listing the material properties used for 6061-T6 aluminum. The principal properties, taken from Reference 2, are provided in Table 7-1.

Table 7-1. Material Properties for 6061-T6 Aluminum

PROPERTY	VALUE
Density	0.098 lb-in^2
Elastic Modulus	10.0 Msi
Ultimate Tensile Strength	42 ksi
Yield Tensile Strength	36 ksi
Ultimate Shear Strength	27 ksi
Coefficient of Expansion	13.0 x 10^{-6}/°F

The conical shell is divided into forward and aft sections that are separated during on-orbit operation. The forward section of the shell receives the largest loading, particularly at its aft station, during reentry. This section was designed for an axial load of 77,010 pounds (1.5 by 3400 pounds by 15.1 g) and, based on the aerodynamic predictions in Reference 2, a pressure of 12.5 psi ultimate (1.5 x 8.3 psi). The sizing analysis was accomplished using Reference 3, since it allows both the shell and frames to be directly determined. The shell was initially considered to be monocoque and then later converted to sandwich based on maintaining the required flexural rigidity. The dimensions used for the analysis are shown in Figure 7-6.

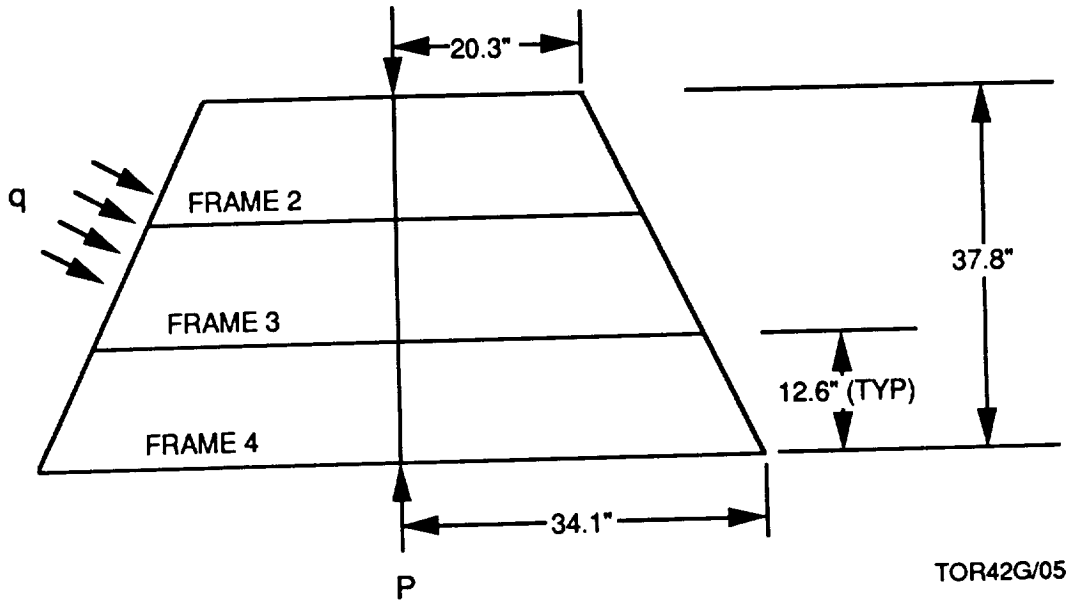

Figure 7-6. Forward Conical Shell Dimensions

The sandwich shell design which resulted from this analysis has a face thickness of 0.030 inch and a honeycomb core thickness of 0.5 inch. A typical cross-section for the intermediate frames is depicted in Figure 7-7.

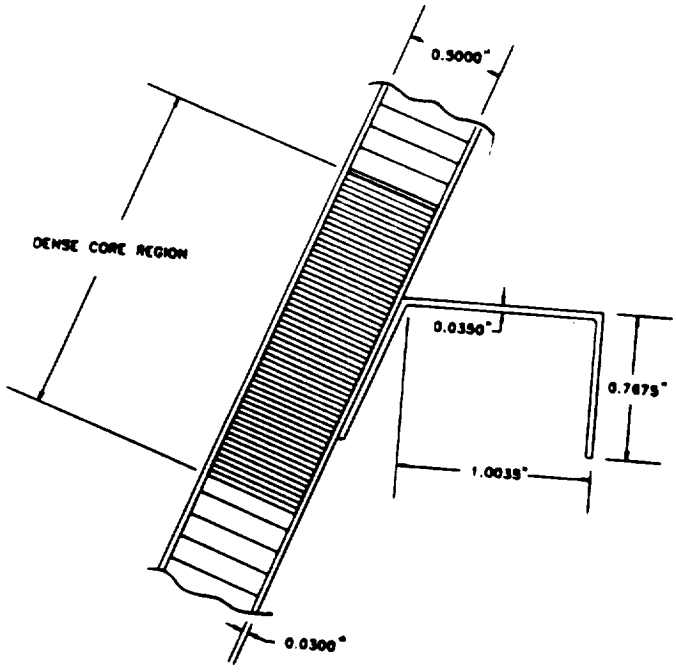

Figure 7-7. Typical Intermediate Frame Cross-Section

For the major frame at the aft end of the forward section, the load from the truss supports was assumed to be placed on the frame at an angle of 36 degrees from the axis of symmetry. Converting this to a radial in-plane load, one obtains a radial load of 261 lb-in acting on a ring diameter of 34.1 inch. This yields a tensile axial load in the ring of 8900 pounds, which requires an area of 0.212 in^2. The resultant calculated frame weight is 4.45 pounds; however, this weight was doubled to account for local buildups in cross-section in order to carry concentrated loads from the truss and latch systems.

The forward payload attach ring was calculated by drawing a ring with reasonable geometry and then analyzing it to ensure that it was structurally sound. The selected design has an area of 0.691 in^2 and a weight of 7.15 pounds. The aft conical shell and its associated frames were designed in a similar manner. Sketches of the results obtained are not provided here, but the resulting weights are presented in Figure 7-8.

C.G. CALCULATION				
Total #	X	Y	Z	
556	0	0	47.9	

Component MAIN STRUCTURE	Mass	X	Y	Z
NOSE CAP				
MONOCOQUE SHELL	10	0	0	9
CRUSHABLE HONEYCOMB	3	0	0	5
HONEY COMB BULHEAD	1	0	0	9
CONICAL SHELL				
SANDWICH SHELL(0.5 *.03)	93	0	0	48
FRAME 1	6	0	0	63
FRAME 2	7	0	0	63
FRAME 3	8	0	0	63
FRAME 4	9	0	0	40
PRIMARY LONGERON	30	0	0	63
SECONDARY LONGERON	15	0	0	63
EQUIPMENT SUPPORTS				
ASTROMASTS	6	0	0	35
AFT TANKS	6	0	0	35
PAYLOAD RING	18	0	0	40
PAYLOAD SUPPORT	3	0	0	25
FORWARD TANK	6	0	0	45
FORWARD COVER	20.00	0	0	45
TRUSS SYSTEM				
TUBES (6)	17.00	0	0	60
END FITTINGS	2.40	0	0	60
SHEAR WEBS				
SHEAR WEBS	4.00	0	0	30
STIFFENERS	8.80	0	0	30
CAPS	8.15	0	0	30

EXTENDED STRUCTURE				
AFT TANK SUPPORT RING	12.00	0	0	68
RADIAL SHEAR WEBS (3)	21.00	0	0	78
AFT COVER	15.00	0	0	87
MAIN BEAMS (3)	50.00	0	0	88
SECONDARY BEAMS (3)	30.00	0	0	88
CROSS BEAMS (3)	10.00	0	0	88
CROSS BEAMS (3)	27.60	0	0	78
FORWARD COVER	20.00	0	0	89
PARACHUTE ATTACH FITTINGS	24.00	0	0	89
LOCKING MECHANISM	15.00	0	0	88

Figure 7-8. Structural Mass

The radial shear webs are vital to providing solid support for the payload canister under axial loading, and in general, tying the entire internal RRS structure together. These shear webs are only attached to the RRS forward section since they stay with the payload canister during on-orbit operation. The basic geometry of each of the shear webs is shown in Figure 7-9.

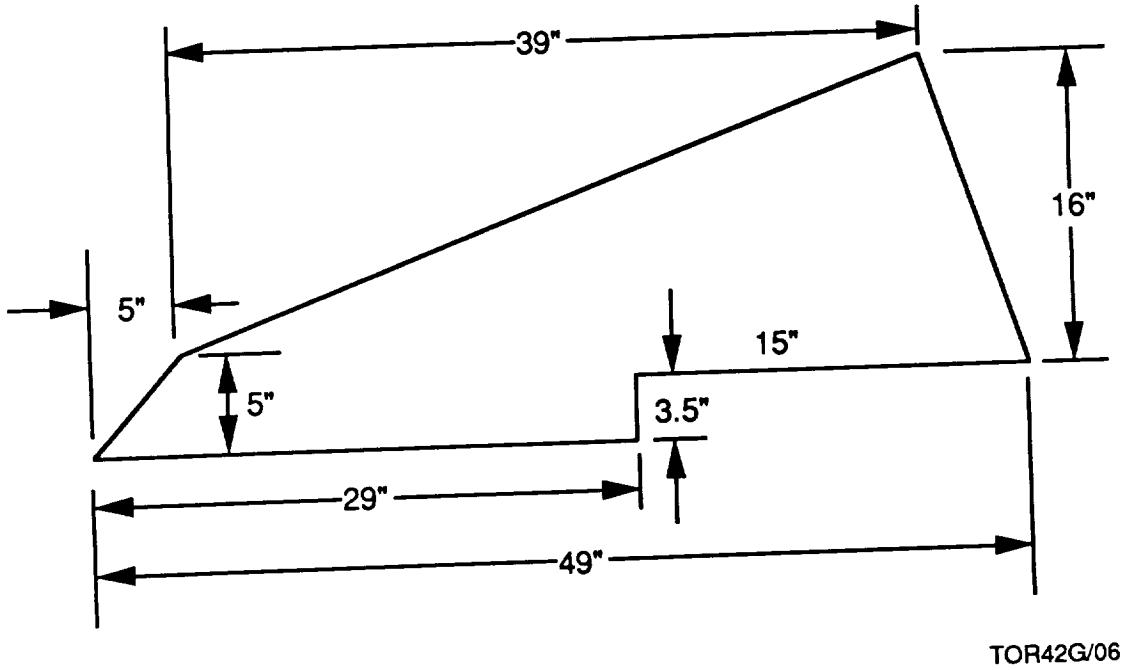

Figure 7-9. Radial Shear Web Geometry

Assuming that the total axial load is carried by the shear webs, the total shear load is 77010/3 = 25670 pounds. Based on the overall length of 49 inches, shown in Figure 7-9, and an allowable shear strength of 27 ksi (Table 7-1), the required shear web thickness is 0.019 in. However, to account for lightening holes and stress concentrations, the shear web thickness is conservatively selected as 0.038 in. This yields a total weight for the three shear webs of approximately 4 pounds.

For the attachment of the shear webs to the payload canister and the conical shell, the two back-to-back angles are mechanically attached as shown in Figure 7-10. The cross-sectional area of these stiffeners is 0.33 in^2, giving a total weight of 8.8 pounds. For the caps, which assist the truss support system in carrying axial load, an area of five times the above value, or 1.65 in^2, was conservatively assumed, providing a total weight for the caps of 8.15 pounds.

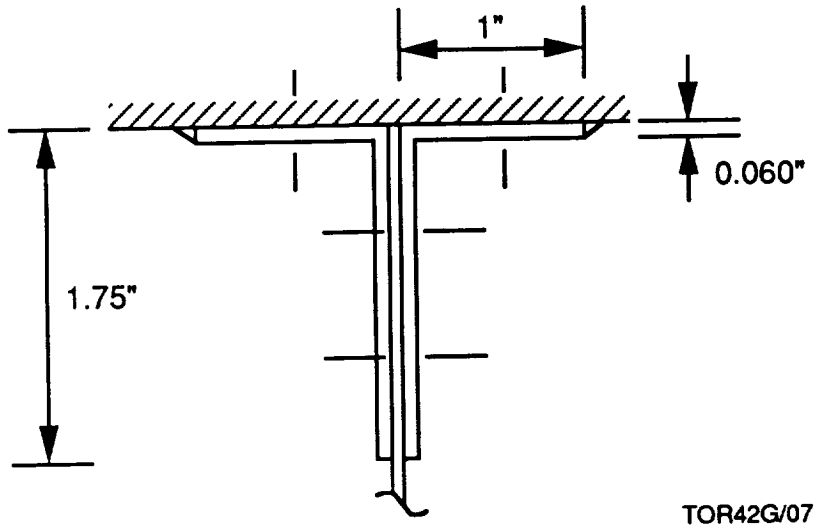

Figure 7-10. Attachment of Radial Shear Web to Payload Canister and External Shell

Truss Support System, Figure 7-11, presents the overall geometry of the truss support system. The truss tubes provide an effective means for resisting lateral and torsional loads, but more importantly, they act in conjunction with the shear web caps to form an integrated system for resisting axial loading. The estimated overall weight of the payload to be supported by this system is 750 pounds. Thus, the ultimate design load for this case is 1.5 by 15.1 g by 750 pounds, or a total of approximately 17,000 pounds. Each truss member can be shown to be 30.26 inches long. Assuming that the truss must be able to carry about 75% of the payload, each of the six truss members can be shown to carry about 10,720 pounds. Optimum structural design then produces a truss tube design having a diameter of 1.375 inches and a wall thickness of .036 inches, giving a weight for each tube of 2.77 pounds. The total tube weight is then 16.6 pounds. Assuming a reasonable design for end fittings, the total of 12 end fittings weighs approximately 2.4 pounds.

To determine the size of the payload attach ring shown in Figure 7-11, a very conservative design approach was used. Even though the ring will most likely be compressed against the payload during ascent, reentry, and parachute deployment, it was designed as though it carries a tensile load, i.e., with six concentrated radial forces. Three of these forces are due to the shear web

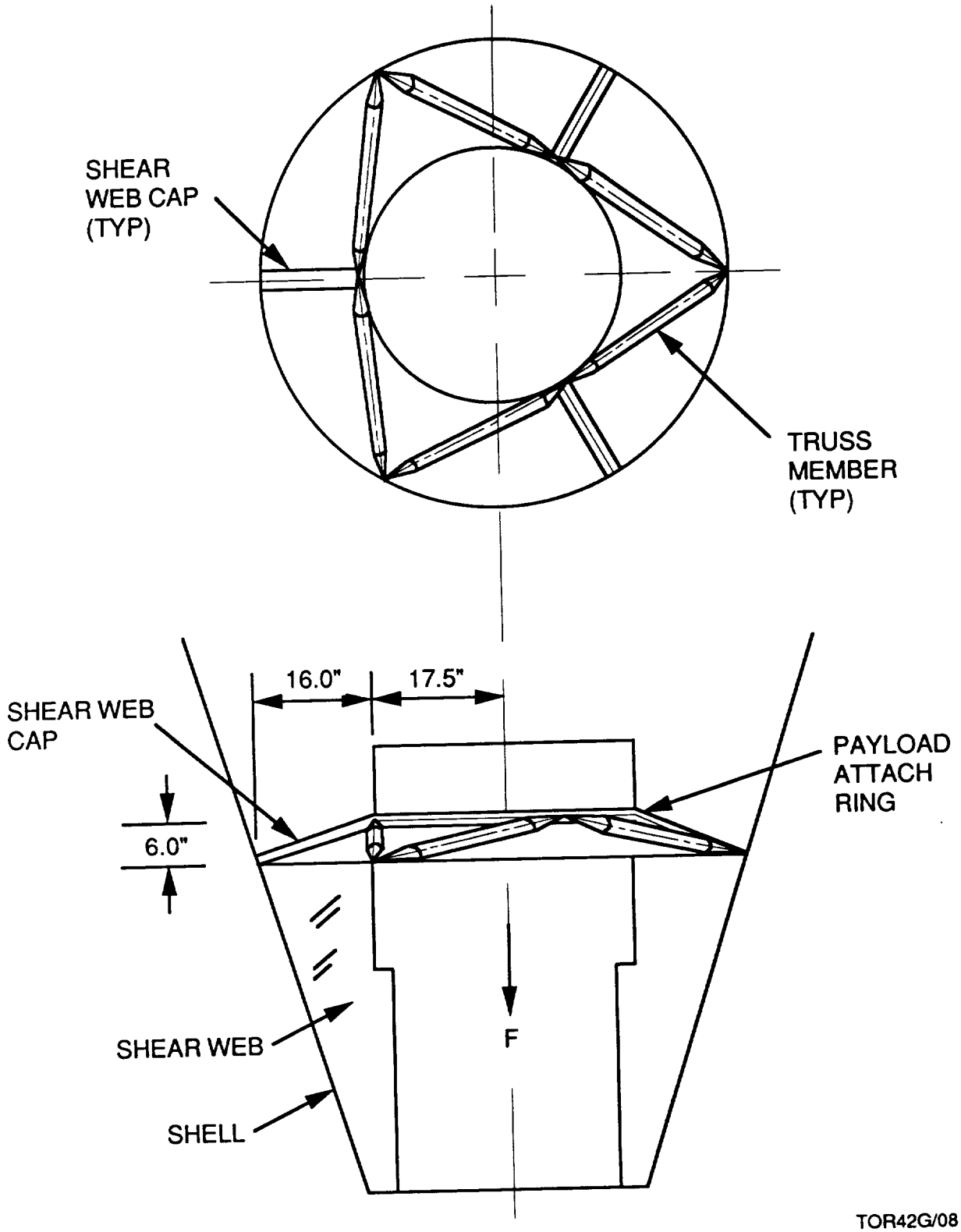

Figure 7-11. Shear Web Cap/Truss System

caps (15,115 pounds/cap), and three are due to the truss attach points (7,990 pounds/point). The ring was then analyzed using formulas from Reference 5, and it was determined that a cross-sectional area of 1.64 in^2 is required, which yields a ring weight of 17.7 pounds.

The aft structure consists of the primary beams, the cross beams, secondary beams, outer ring, and aft cover. To develop the beam loads, it is convenient to first consider the secondary beams and the cross beams before turning to the analysis of the primary beams. There are three primary loads to consider depending on the beam. The primary load condition for the secondary beams is the 1.5 g axial load in an artificial g mission or the 15.1 g deceleration. It was assumed that the weight distribution between the main and deployed modules is 50-50 for the artificial g load calculations. The main beams must be sized to withstand the launch loads of 5.8 g with full propellant tanks. The cross beams are sized by the 1.5 g artificial gravity mission.

Using a standard I-beam design, it was determined from Reference 6 that a 3-inch depth and an area of 2.17 in^2 would suffice. This yields total weights of 49.7, 30.0, and 9.7 pounds for the primary, secondary, and cross beams, respectively.

To complete the design of the aft structure, sizing analyses for the outer ring and aft cover (a lightweight sandwich plate) were also performed. The resulting combined weight of these items was calculated to be 40.8 pounds.

7.4 Equipment Supports

The equipment supports comprise a small part of the overall structure and, consequently, not much effort was placed on designing them with a high level of accuracy. The major structure in this category consists of the payload supports, Astromast supports, battery supports, electronics support, aft tank supports and the forward tank plus payload support.

There are three payload supports, each having a geometry depicted in Figure 7-12. These are envisioned as being built-up areas in the radial shear webs, so as to provide additional axial and lateral payload restraint. The three supports acting together are sized to accommodate at least 40% of the payload weight (approximately 750 pounds) under the 15.1 g reentry condition. This requires a stiffener area of 0.065 in^2. However, to ensure that buckling is not a problem, this was conservatively increased by a factor of 3. The final value calculated for the weight of the three stiffeners is 1.5 pounds.

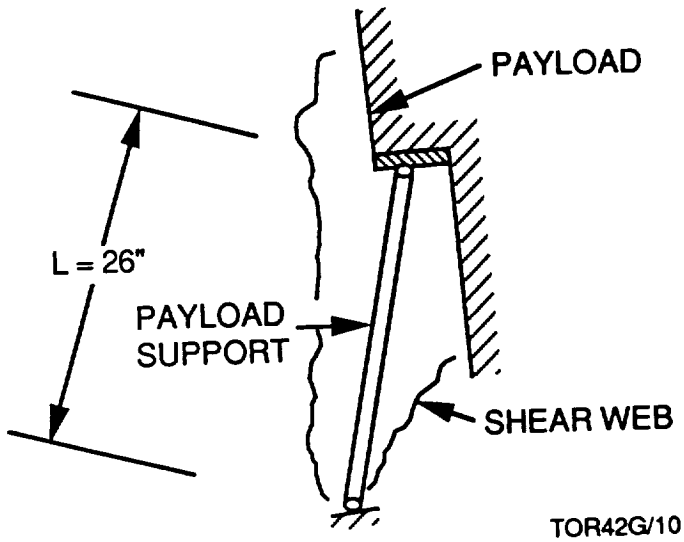

Figure 7-12. Payload Support

The Astromast supports are similar to the above except that the length is 29 inches. Since each Astromast weighs approximately 120 pounds, the ultimate design load for each turns out to be 906 lb. This resulted in an required stiffener area of 0.026 in^2, which was again increased by a factor of 3 to eliminate the potential for buckling. Thus, the final calculated weight is 0.6 pound.

Aft tank supports were not analyzed in any degree of detail, but it was assumed that each tank could be supported by no more than 2 pounds of structural weight. The forward tank plus payload supports were calculated in a manner shown earlier for the payload supports, and the resultant weight is 2.3 pounds. All of the above weights are detailed in the weight summary.

7.5 Nose Cap

It is expected that the nose cap will be crushed on landing. The final design concept is portrayed in Figure 7-13. The external shell is monocoque since it need not be very thick, being supported by the crushable honeycomb that takes the landing shock. According to Reference 2, the pressure at the stagnation point during reentry will be 39.4 psi, which yields an ultimate design pressure of 59.1 psi. Behind the crushable honeycomb, but below the payload, is a honeycomb bulkhead which seals off the payload area provides an insulation barrier. It was determined that a nose cap 0.050-inch thick will weigh 9.5 pounds. A reasonable honeycomb bulkhead was estimated to be 2 pounds, and the crushable honeycomb core material was estimated to be 3.0 pounds based on the information given below.

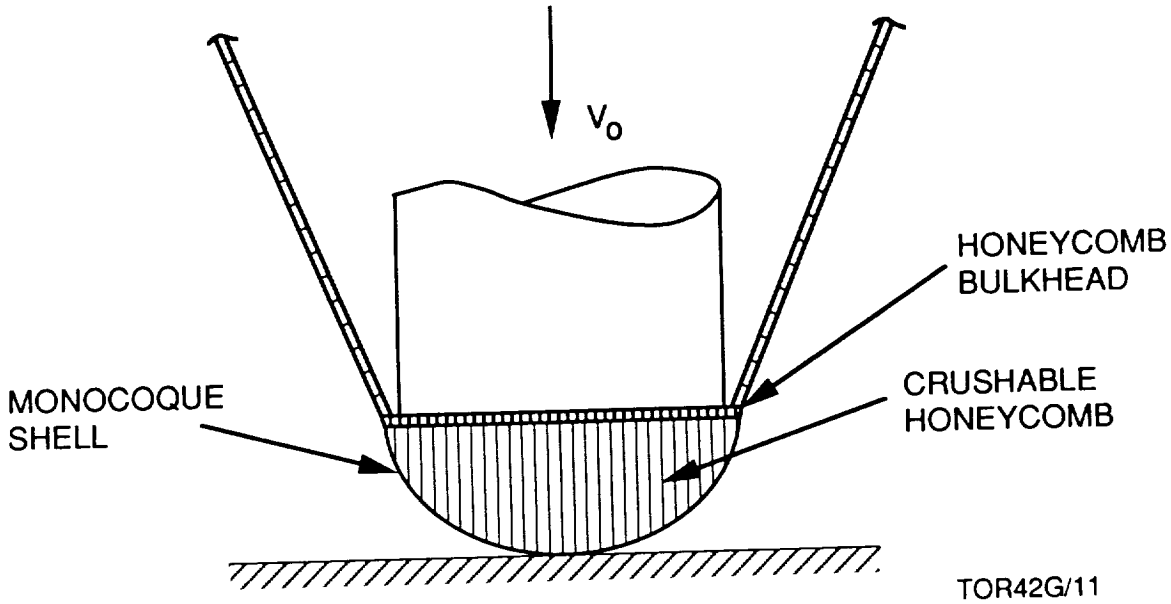

Figure 7-13. Nose Cap Design

To assess the performance of the crushable honeycomb, an analysis was conducted that allows one to determine the dynamic response of the vehicle for a normal impact on the nose at different impact velocities. One of the characteristics of crushable honeycomb is that it can maintain a constant crushing force for given cross-sectional area being crushed. In the present case, however, the cross-sectional area being crushed increases as deformation progresses. The nose geometry and nomenclature used is the distance already crushed. Based on Newton's second law of dynamics, if v_o is the initial velocity and v the current velocity, it can be shown that

$$1/2*M*(V**2-V_O**2)= -\int F(s)ds \quad (1)$$

where m is the total RRS mass, and F(s) is the crushing force, which can be defined as

$$F(s) = f_{cr}A(s) \quad (2)$$

Here f_{cr} is the crushing stress and A(s) is the local area of the crushed "footprint". From Figure 14 one sees that

$$A(s) = \pi*r**2(s) \quad (3)$$

Substitution of Equations 2 and 3 into 1 and setting the final velocity, v, to zero results in the expression

$$V_0**2 = 2*\pi*f_{cr}/m*(RS**2+S**3/3) \quad (4)$$

This gives the first key relation desired. To obtain the second, it is necessary to determine the expression for g, the number of g deceleration, in terms of the crush distance. This is determined by differentiating Equation 4, which results in the expression

$$G= dv/dt/g= -\pi*f_{cr}/(m*g)*(2*R*S+S**2) \quad (5)$$

Note that Equations 4 and 5 are now expressed in terms of the honeycomb crushing stress and the crush distance. Thus it is now possible to develop a plot of these two functions, as shown in Figure 7-14. This can be thought of as the design space for the present problem. In the figure, curves are shown for impact velocities of 5, 10 and 15 ft/sec, together with a curve for the 10 g deceleration constraint. Also shown is a constraint line indicating that there is approximately 9.5 inches of clearance, or available crush distance. To satisfy all of the constraint at the highest impact velocity, one would choose a honeycomb core with a crushing stress as low as possible. Using data from References 7 and 8, it is seen that the core designated as 3/8-5052-.0007 (cell size-material gage) will provide a crushing stress of 25 psi. Referring to Figure 7-14, it can be seen that this design will operate at the point in the design space where the 10 g limit and the 15 ft/sec curve are coincident, and the geometric limit is still satisfied. Hence it appears that the f_{cr} = 25 psi is truly an optimum design for the case analyzed. The case analyzed is probably sufficient for preliminary design, but in future work more attention should be directed to treating the possibility of oblique impact.

7.6 Astromast Dynamics

After the RRS system is placed into orbit, it is converted to its on-orbit configuration through simultaneous extension of the three Astromasts. This is done slowly and deliberately so that no loads and/or dynamic response of any consequence develop. As soon as the Astromasts are fully extended, a small rocket motor at the aft end of the aft RRS module fires, and the system begins to rotate. After reaching the angular velocity associated with the desired artificial gravity environment (less than 1.5 g), the rocket motor is turned off, and the system then reaches its steady-state mode of on-orbit operation.

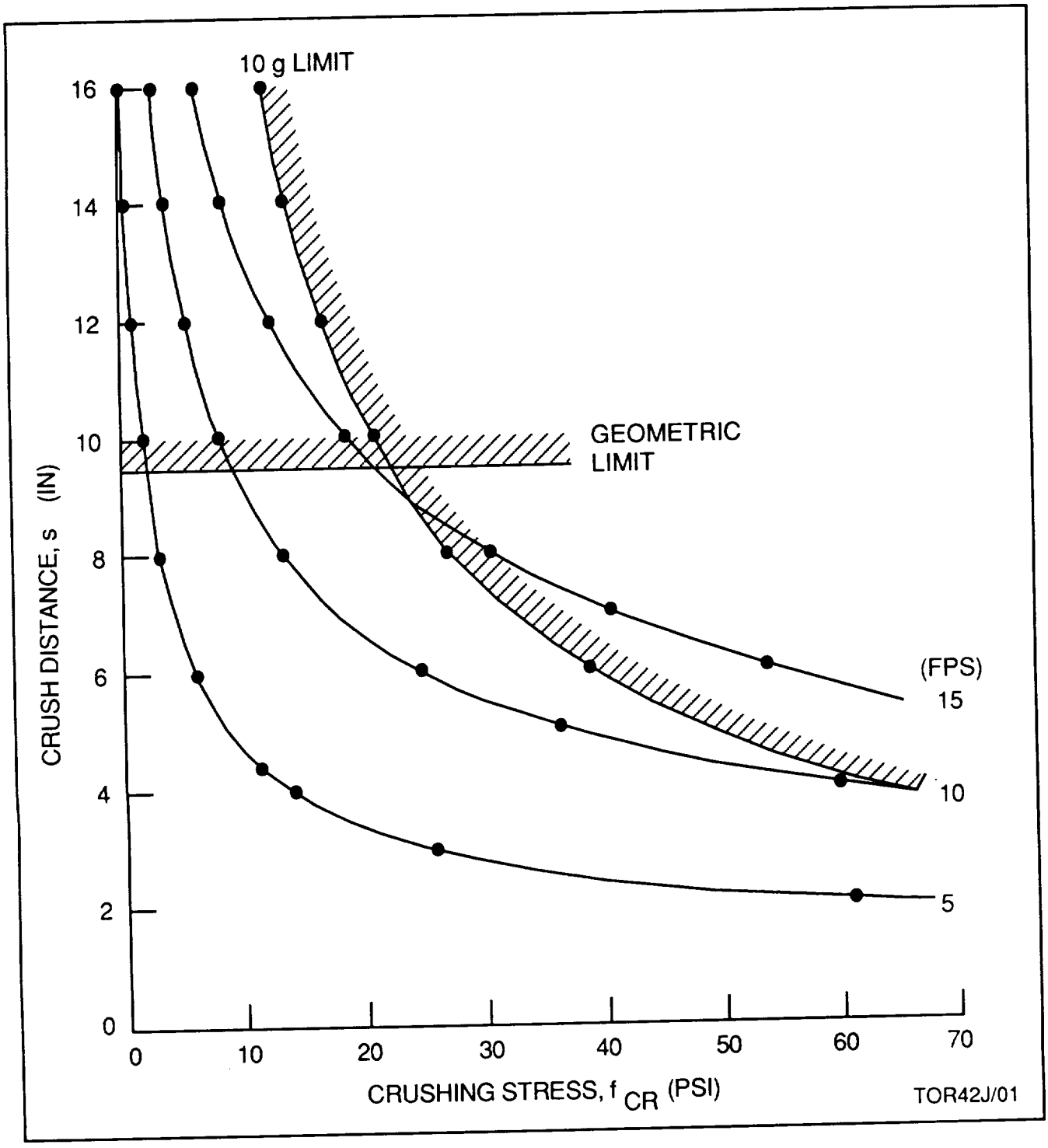

Figure 7-14. Crush Distance Versus Honeycomb Crushing Stress

In order to determine the forces involved and the overall motion that results during the above scenario, a simplified dynamic analysis was conducted with two degrees of freedom for the Astromast. The forward and aft RRS modules are allowed independent motion, as shown in the idealized model of Figure 7-15. The masses and dimensions used are also shown in the figure.

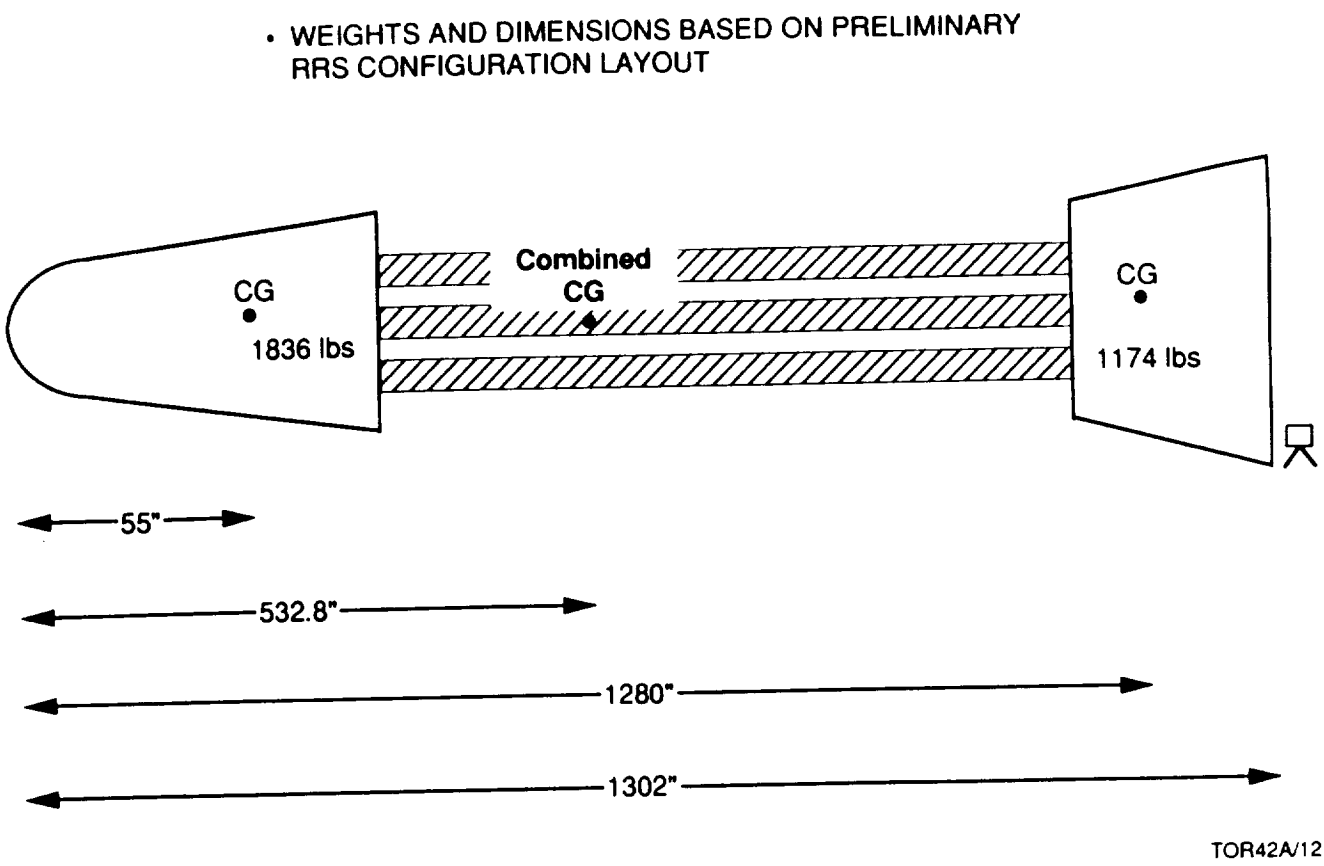

Figure 7-15. Dynamic Loading Analysis Model

The key equations resulting from the analysis are summarized below. In the analysis the two degrees of freedom are combined to develop a single degree of freedom representing relative lateral motion. The natural frequency of the system then becomes

$$W_n 2 = k*(m_1+m_2)/m_1{}^2*m_2 \tag{6}$$

and the displacements y_1 and y_2 can be written as

$$y1(t) = \pi(t) \tag{7}$$

$$y2(t) = -m_1/m_2 *y1(t) \tag{8}$$

where

$$\pi(t)=m_2*L* \S/((m_1+m_2)*W_n{}^2)*[1-1/(\sqrt{(1-q^2)}*t\, e^{-qwnt} *\sin(W_n\sqrt{(1-q^2)}t+\phi)] \tag{9}$$

and

$$q=.005\ ;\ \S=2.605*10^{-4}\quad \phi = \tan^{-1}\sqrt{(1-q^2/q)} \tag{10}$$

To determine the longeron axial load it is first necessary to calculate the bending moment in each Astromast beam, and then add the centifugal loading. The bending moment is given by

$$M(t) = \wedge*E*I/L^2*[y1(t)-Y2(t)] \tag{11}$$

where EI is the bending stiffness of each each Astromast beam; here E is the elastic modulus of the beam longerons, and I the moment of inertia of the beam cross-section.

One of the interesting features of the moment of inertia for the Astromast configuration is that its moment of inertia is independent of the orientation of the bending axis. Based on the orientation, it can be shown that

$$I= 3/2*A*R*R \tag{12}$$

where A is the area of each longeron. Given the above, it can be shown that the stress in longeron 1 (the critical longeron for the orientation shown in Figure 17) can be written as

$$\text{stress} = m1*l1*\Omega*\Omega/(9*A)-2*M/(3*A*R) \tag{13}$$

Therefore, the force in longeron 1 becomes

$$P = m1*l1*\Omega*\Omega/9 - M/1.5*R \tag{14}$$

It can be shown that this indeed produces higher loads than for longerons 2 and 3.

Other results of interest are the angular velocity of the system, given by

$$\Omega(t) = t*\S(t) \tag{15}$$

and the angular acceleration

$$\S(t) = F*(l2+d)/(m1*L^2_1 + m2*L^2_2) \tag{16}$$

Finally, the time required to accelerate m_1 to 1.5 g is

$$t = \sqrt{[1.5*g/(l1*\S(t)*\S(t))]} \tag{17}$$

The above equations were coded into a small Fortran program and the displacements and forces computed. Figure 7-16 shows the displacements y_1 and y_2 for a duration of 4000 seconds. A more detailed view of the same plot for the first 400 seconds is shown in Figure 7-17. The difference between these two displacements is proportional to the bending moment in each Astromast. The axial load in the critical longeron is shown for the 4000 second time period in Figure 7-18. These plots are shown relative to the upper and lower bound allowables; the upper bound is based on tension and the lower on buckling, or geometric instability. In Figure 7-18 it is evident that the longeron load is continually increasing while the small thruster is firing. It is worth noting, however, that the 1.5 g acceleration is achieved at 4257 seconds, and at this time the thruster is turned off and the longeron loads will then stabilize at a value of 332 pounds. Therefore, no Astromast strength problems will arise based on the present analysis.

It is realized that in the future the above analysis should be updated to account for more general response. Such an analysis should include all six possible rigid body degrees of freedom and introduce Euler angles for description of the rotational motion. In addition, several bending and torsional modes should then be superimposed to provide a more general understanding of the structural dynamic response.

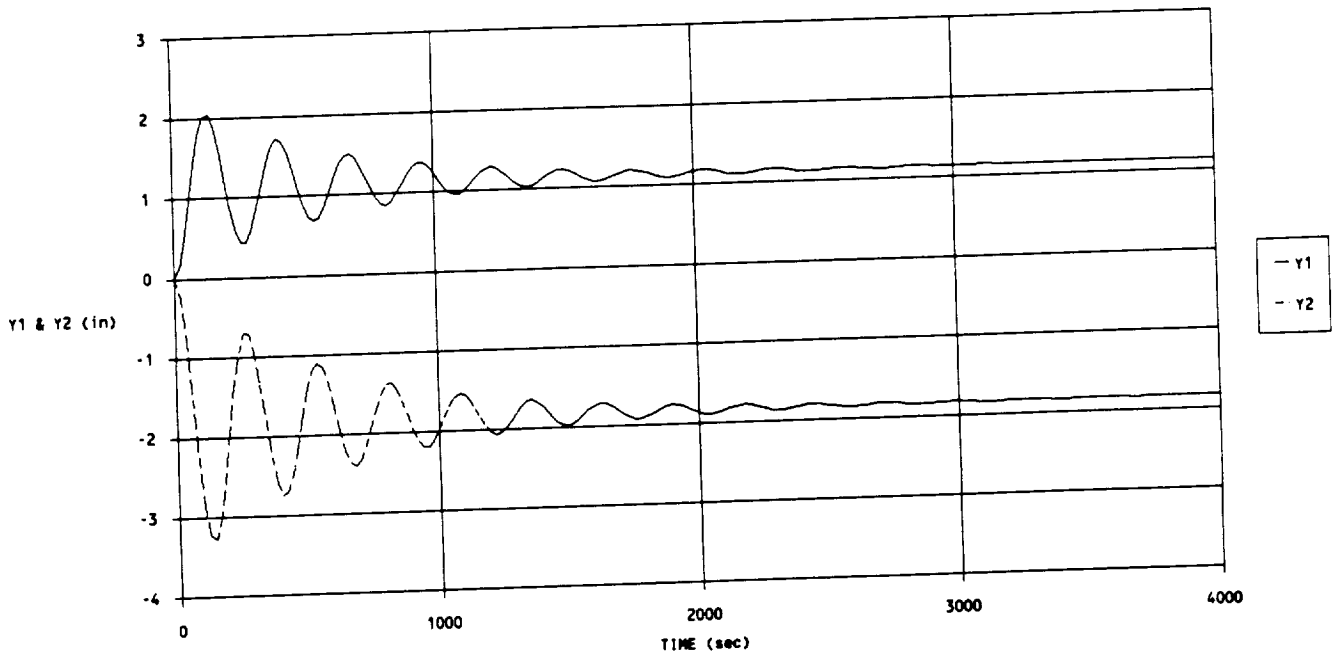

Figure 7-16. Structural Deformation Results

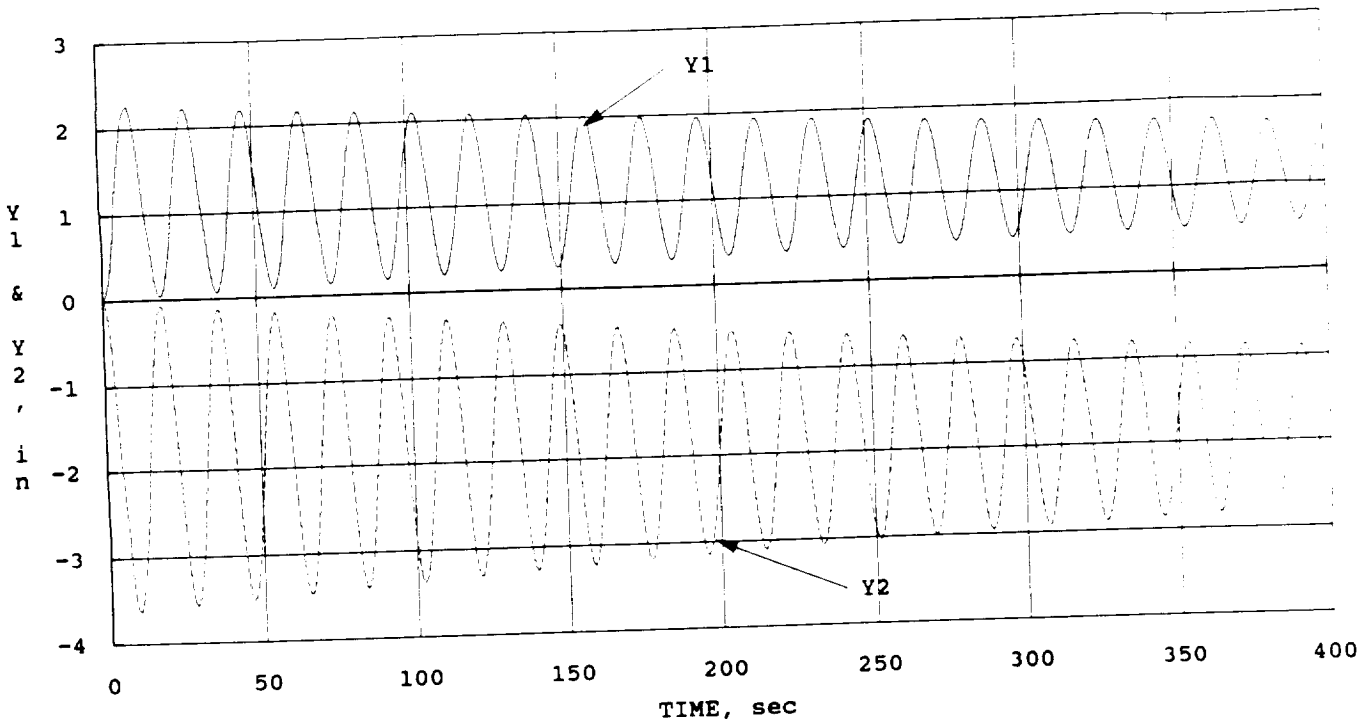

Figure 7-17. Structural Deformation Results - Detailed View

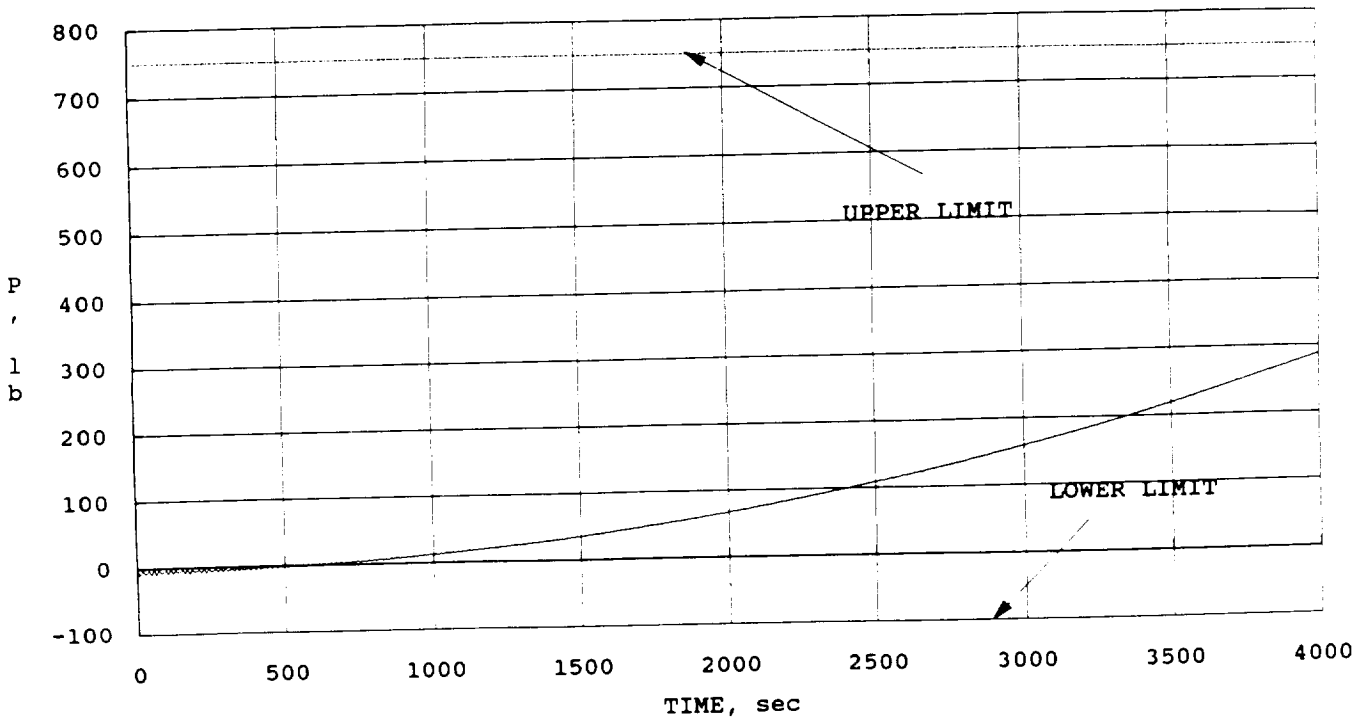

Figure 7-18. Comparison of Longeron Loads With Allowables

8.0 CONCLUSIONS/RECOMMENDATIONS

The configuration trades and design analyses have confirmed the basic feasibility of the SAIC design approach. The key aspects of the design, the Astromast deployment of two halves of the vehicle, the ballistic reentry shape, and the determination of the vehicle mass properties for both maximum spin radius and de-orbit conditions were completed. Additional analysis work will be performed in modeling of the Astromasts using a finite element model as well as refining the weight of the structural subsystem.

References

1. Swenson, B. L. et al., "A Conceptual Design Study of the Reusable Reentry Satellite," Phase A Study, Section J -- Attachment J-3, NASA Ames Research Center, (date unknown).

2. Weinberg, S., "Inputs to RRS Structural Analysis," Technical Memorandum to W. Loomis, November 17, 1989.

3. Hess, T. and R. Garber, "Stability of Ring-Stiffened Conical Shells Under Simultaneous Lateral Pressure and Axial Compression," General Electric Co., Valley Forge, PA, GE Report R58SD226, April 1958.

4. MIL-HDBK-5B, Military Standardization Handbook, "Metallic Materials and Elements for Aerospace Vehicle Structures," 15 August 1974.

5. Roark, R. J., Formulas for Stress and Strain, McGraw-Hill, New York, 1954.

6. Shanley, F. R., Strength of Materials, McGraw-Hill, New York, 1957.

7. Hexcel Corporation, TSB 120, "Mechanical Properties of Hexcel Honeycomb Materials," 1988.

8. Hexcel Corporation, TSB 122, "Design Data for the Preliminary Selection of Honeycomb Energy Absorption Systems," 1989.